ALMA MATER STUDIORUM
UNIVERSITÀ DI BOLOGNA

SCHOOL OF ENGINEERING

SECOND CYCLE MASTER'S DEGREE in
AEROSPACE ENGINEERING
Class LM-20

Ephemeris reconstruction of asteroid 65803 Didymos using astrometric and radiometric data

Thesis in:
Spacecraft Orbital Dynamics and Control

Supervisor:
Prof. RICCARDO LASAGNI MANGHI

Defended by:
LORENZO CARLETTI

ACADEMIC YEAR 2022/2023

Abstract

The planetary defense efforts reached a significant milestone with the success of NASA's Double Asteroid Redirection Test (DART) mission. The mission effectively demonstrated the kinetic impactor technique as a viable means for asteroid deflection by impacting the DART spacecraft on Dimorphos, the minor component of the Didymos binary asteroid system. Although the impact's effects on the mutual orbit of the asteroids have been measured, its effect on the system heliocentric orbit, described by the momentum enhancement parameter $\beta_{\odot}$, is yet to be determined. Scheduled for launch on October 2024, ESA's Hera mission aims to investigate the Didymos system in the aftermath of the DART impact, through a detailed characterization of the physical properties of the asteroids and of the impact crater. In this work, we present a reconstruction of the heliocentric trajectory of Didymos through an orbit determination process that uses currently available astrometric observations and simulated measurements from future ground-based observations, and radiometric measurements collected by the Hera mission. We find that current measurements are insufficient to estimate $\beta_{\odot}$ and separate its effect from other non-gravitational forces, such as the one induced by the Yarkowsky effect. Therefore, by conducting a covariance analysis, we explore the observability of $\beta_{\odot}$ and other critical parameters related to the non-gravitational motion. Specifically, we assess how the accuracy of such parameters is influenced by the frequency and nature of the various observations collected throughout the Hera mission, namely astrometric observations, range, and ΔDOR measurements. We show that combining range and ΔDOR observations substantially increases the signal-to-noise ratio of the estimated parameters and significantly reduces the position uncertainties on the whole estimation arc.

Contents

List of Figures

List of Tables

Chapter 1

Introduction

In the past four decades our knowledge of the Solar System has greatly expanded as interplanetary exploration spacecrafts have provided close-up views of all of the planets, as well as collection of smaller bodies such as natural satellites, asteroids and comets. In this regard, considerable attention has been given to the observations of Near-Earth Objects (NEOs), leading to the discovery of many potentially hazardous objects, mainly asteroids, which could impose a potential threat in case of close approach to our planet. Indeed, planetary defence concerns have been the subject of active scientific research and global governance activity for many years, through cooperative international efforts to surveil and map the orbits of NEOs and assess their sizes. In 2013 these efforts led to the formation of the International Asteroid Warning Network and the Space Mission Planning Advisory Group [1]. Moreover, in 2016 NASA established the Planetary Defense Coordination Office to manage its ongoing mission of planetary defense, which does not include only the detection, tracking and characterization of PHOs, but also the study of strategies for response to an actual impact threat. The campaign reached recently an important milestone with the success of the DART (Double Asteroid Redirection Test) mission where a spacecraft

impacted on the asteroid Dimorphos, a natural satellite of the larger Near Earth Asteroid (NEA) Didymos, which will be the focus of this thesis.
In this work we will present a reconstruction of the heliocentric trajectory of Didymos, which represent a key step for validating the kinetic impactor concept for planetary defence. This analysis was conducted through an orbit determination process which used currently available astrometric measurements and simulated data for future ground based observations, and radiometric measurements for the Hera mission. Furthermore, we will explore the observability of the velocity variation imparted on the Didymos system by DART's impact, and the magnitude of the non-gravitational effects acting on the asteroids through the estimation of the parameters A_2 and $\beta_\odot$. Specifically, we will conduct a covariance analysis to assess how the accuracy of such parameters is influenced by the type and frequency of the various observation collected throughout the Hera mission.
This thesis work is therefore structured in the following way. In Chapter 1 we contextualize the Didymos system by presenting its characteristics and by briefly introducing the DART and Hera missions. In Chapter 2 we discuss the typical measurement techniques employed for the ephemerides reconstruction of small bodies and for spacecraft (s/c) tracking, as well as some considerations on the astrometric observations of the Didymos system reported to the Minor Planet Center (MPC). Chapter 3 introduces the Orbit Determination (OD) process and the model validation. In Chapter 4 we describe the procedure followed in this analysis, and the simulation set-up implemented. In Chapter 5 we explain the reasoning behind the measurements simulation and we show how we can derive radiometric observations (with the corresponding uncertainties) for Didymos exploiting the presence of the Hera s/c, which will visit the asteroid system in 2027. In Chapter 6 we show the result of the covariance analysis and the expected measurability of the parameters. In Chapter 7 we perform a sensitivity analysis to assess how

the solutions are affected by the number and frequency of radiometric observations. Finally, we draw the conclusions and we summarize the results and considerations derived in this work.

1.1 Didymos Binary Asteroid System

The Didymos asteroid system, subject of this work, is a binary system composed of the asteroids Didymos, the central body, roughly 780 meter in diameter, and its smaller moon Dimorphos (160 meter in diameter). Didymos, now designated with the MPC code 65803, was discovered in 1996, while the presence of Dimorphos was confirmed on Nov. 23, 2003 from the analysis of optical light curves [2]. Didymos, categorized as a NEA, belongs to the Amor subgroup based on the characteristics of its orbit. An asteroid is classified as an Amor if its perihelion falls within the range of 1.02 to 1.03 AU, thus never crossing Earth's orbit. In terms of composition, Didymos is identified as an S-type asteroid, primarily composed of silicate materials and nickel-iron [3]. The key attributes of the binary system are summarized in Table 1.1, along with parameters related to Dimorphos' orbit with respect to Didymos. Following DART's impact, Dimorphos' orbital angular momentum has changed thus resulting in a reduced semi-major axis and orbital period. The values reported in the table refers to the pre-impact state of the secondary asteroid.

Table 1.1. Didymos system physical properties, heliocentric orbital parameters and pre-impact mutual orbit parameters.

Parameter	**Symbol**	**Value**	**Uncertainty (1σ)**	**Unit**
Physical properties[1]:				
Mass of the system	M_{tot}	5.55×10^{11}	0.42×10^{11}	kg
Diameter of the primary	D_p	780	30	m
Diameter of the secondary	D_s	164	18	m

[1]Rivkin et. al. [4]

Parameter	Symbol	Value	Uncertainty (1σ)	Unit
Bulk density of the primary	ρ_p	2170	350	kg m^{-3}
Mean absolute magnitude	H	18.16	0.04	—
Slope parameter	G	0.2	0.02	—
Geometric albedo	ρ_v	0.15	0.04	—
Heliocentric orbit [2]:				
Aphelion distance	Q	2.272	3.76×10^{-10}	AU
Perihelion distance	q	1.013	2.81×10^{-10}	AU
Semi-major axis	a	1.642	2.72×10^{-10}	AU
Eccentricity	e	0.383	1.34×10^{-10}	—
Inclination	i	3.414	1.62×10^{-8}	deg
Ascending nodes	Ω	72.988	2.19×10^{-7}	deg
Argument of perihelion	ω	319.579	2.51×10^{-7}	deg
Mean anomaly	M_0	152.705	4.40×10^{-8}	deg
Orbital Period	P	2.105	5.23×10^{-10}	Earth years
Mutual orbit (pre impact)[3]:				
Semi-major axis	a_s	1.21	0.03	km
Orbital Period	P_s	11.922	3.10×10^{-6}	hour
eccentricity	e_s	<0.03	—	deg

1.2 The DART mission

In recent years, Didymos and Dimorphos have been in the spotlight since the asteroid system was selected as the target of the DART mission, whose primary goal was to demonstrate the kinetic impactor (KI) as a viable technique for planetary defense. The concept is to deflect an asteroid trajectory by impacting a spacecraft on its surface at high speed. Specifically, the DART s/c goal was to impact Dimorphos and demonstrate to be able to change its orbital period about Didymos by increasing its orbital angular momentum. In its journey, DART was also accompanied by LICIACube, a 6U CubeSat, which was deployed right before the impact to provide on-site documentation of the collision and immediate aftermath.

[2] `https://ssd.jpl.nasa.gov/tools/sbdb_lookup.html#/?sstr=Didymos`. Reference epoch: 13-SEP-2023 TDB

[3] Rivkin et. al. [4]

On September 26 2022, DART successfully impacted Dimorphos, changing its orbital period from $11.922 \pm 3.10 \times 10^{-6}$ h to 11.372 ± 0.017 h, as estimated through the analysis of ground-based lightcurves [5]. This corresponds to a period variation of 33 minutes, which greatly exceeds the expected 7 min period change calculated for the case of a simple momentum transfer. The main reason for this large difference is the ejecta that formed after the impact. The mass expelled from the secondary asteroid carried a substantial amount of momentum compared with what the DART spacecraft was carrying. This additional momentum can be quantified in terms of a momentum enhancement parameter β defined by the momentum balance of the kinetic impact [6]:

$$M\Delta\vec{v} = m\vec{U} + m(\beta - 1)(\hat{E} \cdot \vec{U})\hat{E} \tag{1.1}$$

Here, M is the mass of Dimorphos, $\Delta\vec{v}$ is the impact induced change in Dimorphos's orbital velocity, m is DART's mass at impact, $\vec{U}$ is DART's velocity at impact relative to Dimorphos and $\hat{E}$ is the net ejecta momentum direction. Figure 1.1 helps visualizing the problem, together with a picture of Dimorphos's ejecta captured by the Webb telescope[4]. With the current information available, it is not possible to measure directly the 3 components of the $\Delta\vec{v}$. However, the knowledge of the orbital period variation can tell us how the along-track component (velocity component in the direction of Dimorphos's orbital velocity) of Δv has changed. An expression for β in the along-track direction $\hat{e}_T$ can be derived from Equation 1.1:

$$\beta = 1 + \frac{\frac{M}{m}(\Delta\vec{v} \cdot \hat{e}_T) - (\vec{U} \cdot \hat{e}_T)}{(\hat{E} \cdot \vec{U})(\hat{E} \cdot \hat{e}_T)} \tag{1.2}$$

Cheng et. al. [6] ultimately derived a value for β of $3.61^{+0.19}_{-0.25}$ with 1σ confidence on the basis of the observed impact-induced period change

[4] `https://hubblesite.org/contents/media/images/2022/047/01GE39QQCQ52JSF02RYJYCHH7J`

and numerical simulations. In light of these results, the DART mission successfully demonstrated not only that an asteroid could be targeted during a high-speed encounter, but also that it managed to affect its trajectory and change its orbital period. However, to fully asses the outcome of the mission, the so called heliocentric momentum enhancement factor $\beta_{\odot}$ still needs to be determined. $\beta_{\odot}$ is the counterpart of the β factor that refers to the heliocentric orbit of the asteroid system. If we assume that the impact causes an instantaneous change in the momentum vector, and that the escaping ejecta travels in the opposite direction to DART's relative momentum, $\beta_{\odot}$ can be defined as [7]:

$$\Delta\vec{p} = \beta_{\odot}\vec{p}_{DART} \tag{1.3}$$

where $\Delta\vec{p}$ is the vector momentum variation of the asteroid and $\vec{p}_{DART}$ is the relative momentum vector carried by DART at the moment of impact. The estimation of this parameter would allow us to determine the momentum variation due to the portion of ejecta that managed to escape the binary asteroid system's gravitational influence, and thus determine how the heliocentric orbit will be influenced. Detectable changes in the orbit will occur on a longer time scale than the change in the mutual orbit period. Furthermore, the combined effects of the impact and debris ejection are in the same order of magnitude of non-gravitational forces such as the Yarkowsky effect. In order to derive this parameter we will then need to propagate our solution some years into the future.

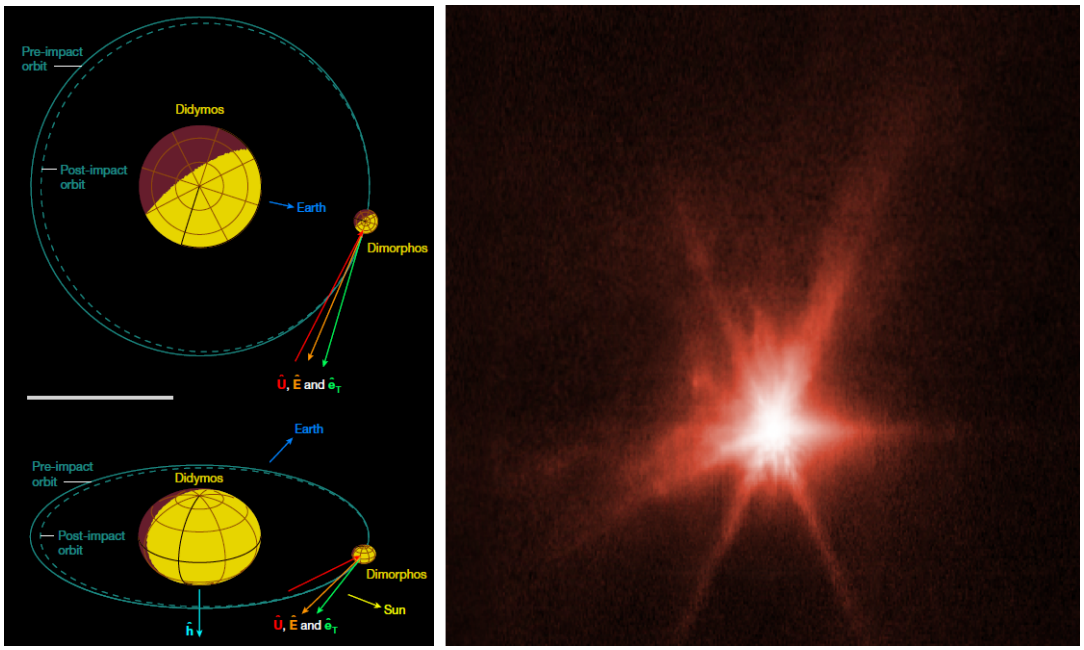

Figure 1.1. Left: schematic of the DART impact geometry. $\hat{U}$ is DART's incident direction, $\hat{E}$ is the net ejecta direction and $\hat{e}_T$ is the along-track direction. The continuous line represents Dimorphos's pre-impact orbit while the dashed line represents the post-impact orbit [6]. Right: dimorphos's ejecta 4 hours after DART impact. Image captured by Webb's telescope infrared camera.

1.3 The Hera mission

The next phase of the planetary defense programme is represented by the Hera mission which is currently under development in the Space Safety Program of the European Space Agency (ESA) and scheduled for launch on October 2024. The mission aims to investigate the Didymos asteroid system with a set of goals that are related to the detailed measurement of the outcome of the DART test, and to the characterization of the asteroid system . Michel et. al. [8] gives a comprehensive list of Hera's goals, which include, a detailed characterization of the

physical properties of Didymos and Dimorphos and of DART's crater morphology, as well as measurement of the momentum transfer efficiency resulting from DART's impact. In order to reach these goals, the Hera s/c will carry 5 scientific instruments and 2 additional CubeSats, Juventas and Milani, that will be deployed at close proximity to Dimorphos and will be in communication with the mother craft through a novel inter-satellite link. Figure 1.2 shows the design of the Hera s/c and the disposition of its payloads.
Launched in a window between between the 8th and 25th of October 2024, Hera is expected to reach the Didymos system on December 2026 and start its scientific operations near the end of January or early February 2027. Figure 1.3 summarizes the Hera concept of operations, which is structured in the following way [8]:

- Early Characterization Phase (ECP, 6 weeks). Hera will follow hyperbolic arcs at distances from the asteroid ranging between 20 to 30 km. During this phase, the global shape, mass/gravity, thermal and dynamical properties of the asteroid will be studied.
- Payload Deployment Phase (PDP 2 weeks). Release of Juventas and Milani and support of their early operations.
- Detailed Characterization Phase (DCP, 4 weeks). Hera will continue to move on hyperbolic arcs, but the distance will be reduced to 8-20 km. During this phase meter-scale mappings of the asteroid will be performed. Moreover, thermal, spectral and interior properties will be analysed.
- Close Observation Phase (COP, 6 weeks). The pericenter distance is reduced to 4 km and, with a total of 12 close flybys, high resolutions investigations of a large fraction of the surface area of Dimorphos (including the DART impact crater) will be performed.
- Experimental Phase (EXP, 6 weeks). In this phase innovative navigation techniques will be experimented to get flybys to lower al-

titudes, down to 1 km or less. The phase, and the Hera mission, will likely end with the s/c landing on one of the two asteroids and providing, in the process, high resolution data on the primary.

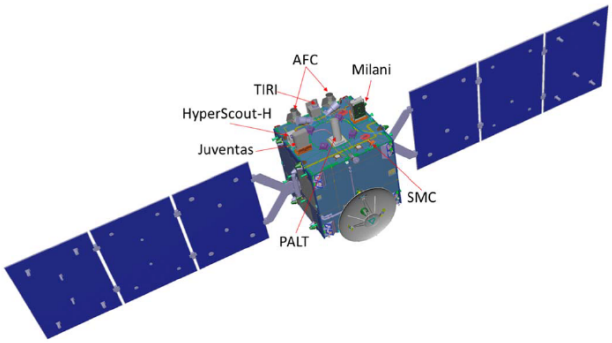

Figure 1.2. Hera spacecraft design with its payloads and their acronyms. AFC = Asteroid Framing Cameras; TIRI = Thermal InfraRed Imager; PALT = Planetary ALTimeter; SMC = Small Monitoring Cameras [8].

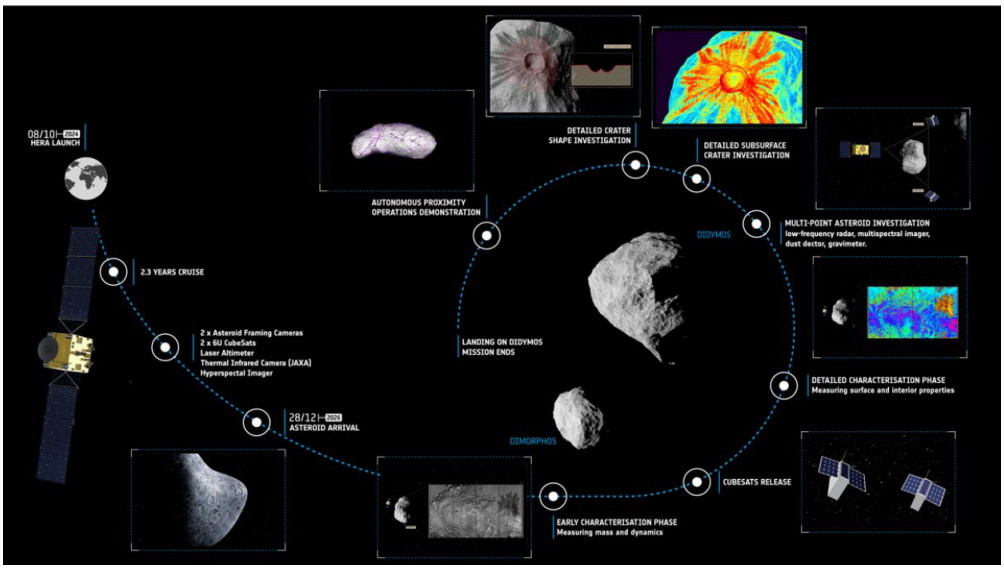

Figure 1.3. Hera mission overview [8].

Chapter 2

Astrometry: optical and radio measurement techniques

Generally speaking, we talk about astrometry to indicate all that is necessary to provide positions and motions of celestial bodies, whether they are natural or artificial. Astrometry includes various fields, ranging from definition of fundamental reference frames and astronomical phenomena, to observational techniques, instrumentation, data processing and mathematical model to take into account all possible sources of uncertainties in the measurements.
Position and velocity of objects in the sky can be determined through different techniques. Celestial objects like asteroids or comets are often observed from telescopes on Earth or in orbit, that collect digital images of these bodies. Radio tracking techniques are mainly used for s/c, with which is possible to establish a communication link with ground stations. In the following sections, an introduction to the most common radiometric and astrometric techniques is presented, highlighting the working principles, how they are collected and the main sources of errors and uncertainties.

2.1 Asteroid optical astrometry

Modern optical astrometry is performed by ground based and space telescopes by imaging celestial bodies using Charge Coupled Device (CCD) detectors, and consists in deriving the object position in the sky in terms of Right Ascension (RA) and Declination (Dec). When an object in the sky has unknown RA and Dec coordinates, a series of images is captured, including the celestial body and the surrounding stars. By interpolating the object's position relative to the stars, whose celestial equatorial coordinates are already established, we can derive the coordinates of the unknown body in the EME2000 frame. The stars with known positions are commonly referred to as reference stars or standard stars. In order to distinguish an asteroid from a star, astronomers take several images few minutes apart. Since asteroids orbit the Sun, they will appear to be moving while switching between the pictures, with the reference stars that will appear instead to be fixed. This technique is called "blinking" [9] and allows to easily spot a moving asteroid after orienting and aligning the images.
Nowadays, computers and dedicated software greatly help astronomers in performing this kind of procedures, allowing observatories to identify large number of unknown asteroids and submit many observations. Moreover, it is evident the importance of using accurate star catalogs. Small bias and inaccuracies in the position of the background stars can lead to errors in the derivation of asteroid's celestial coordinates and, ultimately, larger uncertainties in the reconstructed orbit. For this reasons, the GAIA catalogs have now became the standard for astrometric observations. Other sources of error can be related to the instruments used, i.e. CCD camera and telescope, the brightness of the body and its motion, which can cause detection to be trailed along the direction of motion [10]. All of these effects are taken into account during the pre-processing of astrometric data. The schemes used for this purpose will be discussed in section 3.2.1.

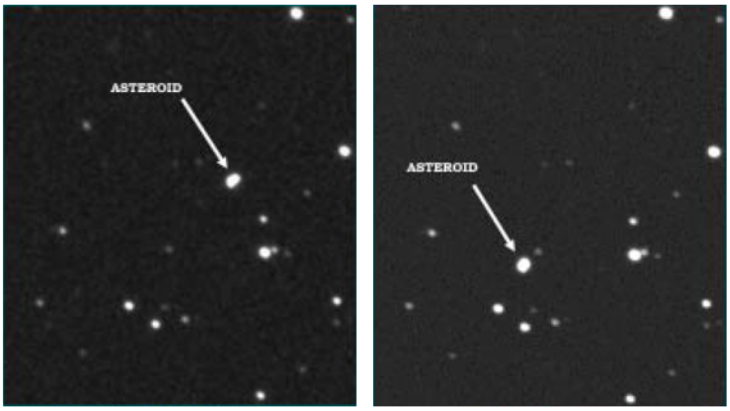

Figure 2.1. Example of CCD images taken 25 minutes apart. From the position of the background stars, astronomers work out the celestial coordinates of the asteroid [9].

2.2 Asteroid Radar Astrometry

Radar astrometry is a technique that provides measurements of range and/or range rate of celestial bodies based on the echos received at the transmitting station. A typical transmit/receive cycle consists of signal transmission for a duration close to the round-trip light time between the radar and the target, i.e., until the first echoes are about to come back, followed by reception of echoes for a similar duration [11]. There exist two types of radar observations. A radar "delay" measurement is the elapsed time for a signal to travel from transmitter to receiver after reflecting off the target. "Doppler" is the frequency-change measured between receiver and transmitter after reflecting off the object, and is related to the net up and down-leg relative velocity of the object. Delay-Doppler provide spatial measurements orthogonal to optical angle measurements with meter-level accuracy, thus allowing for significant improvement in estimates of orbits and ephemerides prediction.

Moreover, with adequate orientational coverage, they can be used to construct geologically detailed three-dimensional models of the body, to define the rotation state precisely, and to constrain the object's internal density distribution[1].

2.3 The radio link

All space missions require some form of telecommunications network with a ground system to transmit to and receive data from spacecrafts. The ESA's tracking station network, also known as ESTRACK, is one of the largest and most sophisticated of such networks and comprises different complexes all around the world, some of which are employed to track deep-space missions, i.e. missions operating at or beyond the orbit of Earth's moon. ESA's Deep Space Antennas (DSA) are located in New Norcia (Australia), Cebreros (Spain) and Malargüe (Argentina). Communication with a s/c is performed within internationally allocated frequency bands, shown in table 2.1. We call uplink a signal that is sent from the ground station to the s/c, while we call downlink a signal sent from the s/c to the ground station.

Band	Uplink frequency [MHz]	Downlink frequency [MHz]
S	2110-2120	2290-2300
X	7145-7190	8400-8450
Ka	34200-34700	31800-32300

Table 2.1. Uplink and downlink frequency bands for deep-space communications [12]

Radio links are used to track the s/c for OD purposes, download telemetry (houskeeping and paylod) and uplink commands to control the s/c. There exist 3 link configurations:

[1] `https://echo.jpl.nasa.gov/introduction.html`

- 1-Way. Only a downlink signal is generated by the s/c by the on board electronics.
- 2-Way. A ground station transmits a signal to the s/c. The s/c receiver locks on and tracks the uplink carrier via a Phase-Locked Loop (PLL). The PLL produces a reference signal which is used to demodulate the uplink commands and generate a downlink signal. The s/c then transmits back the signal to the same uplink ground station.
- 3-Way. Same as 2-Way but the ground station receiving the downlink signal is different from the station that generated the uplink.

In the following sections we briefly discuss the most common techniques for s/c tracking, which will be considered when simulating Hera's radiometric observables.

2.3.1 Range and doppler tracking observables

The so-called range and doppler observables allow to derive position and velocity of the s/c, usually indicated with range ρ and range rate $\dot{\rho}$. Spacecraft range is measured by the round-trip transit time of a ranging signal generated at one of the DSA stations. The delay information is retrieved by evaluating the phase variation between the uplink and downlink signals within a finite number of cycles. To resolve the phase ambiguity, a series of tones with frequencies that are sub-multiples of the carrier frequency are used [13]. S/c topocentric slant range is approximately related to the one-way signal transit time, τ_g, by the expression:

$$\rho = \tau_g c \tag{2.1}$$

where c is the speed of light [12]. Knowing the round-trip time, we can evaluate the s/c range ρ. Information on the s/c velocity can instead be derived by exploiting the Doppler effect, which is the change in

frequency (or wavelength) of a signal emitted from a source moving with respect to the observer. An approximated expression for the received frequency from a s/c receding from Earth is given by:

$$f_r = (1 - \frac{\dot{\rho}}{c}) f_t \tag{2.2}$$

where f_t is the frequency transmitted by the s/c and $\dot{\rho}$ is the instantaneous slant range rate. The quantity $(\dot{\rho}/c)f_t$ is referred to as the Doppler shift. Figure 2.2 illustrates the concept of the Doppler extraction process. The s/c receives a signal at a certain frequency, which will be different from the reference frequency due to the Doppler effect. The difference between the transmitted and received carrier frequencies yields the Doppler tone. A counter then measures the total phase change of the Doppler tone (with resolution up to one-hundredth of a cycle) during the so-called count time, T_c. Each time the phase of the received signal slips one cycle relative to the phase of the transmitted signal, the distance over which the signal has propagated has increased by one wavelength (for instance, 3.6 cm at X-band). The Doppler count thus provide a measure of range change over the count time interval T_c. Doppler observables can provide measurements of a spacecraft's angular position as well. These information are encoded in the diurnal amplitude, which depends on Earth's mean rotation, and the phase of the slant range rate signal. Specifically, the amplitude correlates with the spacecraft's Dec, while the phase is associated with the Ra [12]. Nonetheless, there exist considerably more robust methods for directly measuring angles and angular rates, such as VLBI and ΔDOR.
Range and Doppler measurements are generally affected by clock instabilities, instrumental delays, transmission media dispersion and imperfection in the modelling of the tracking geometry, such as ground station locations or Earth orientation. These effects have to be taken into account when processing and modelling this kind of measurements.

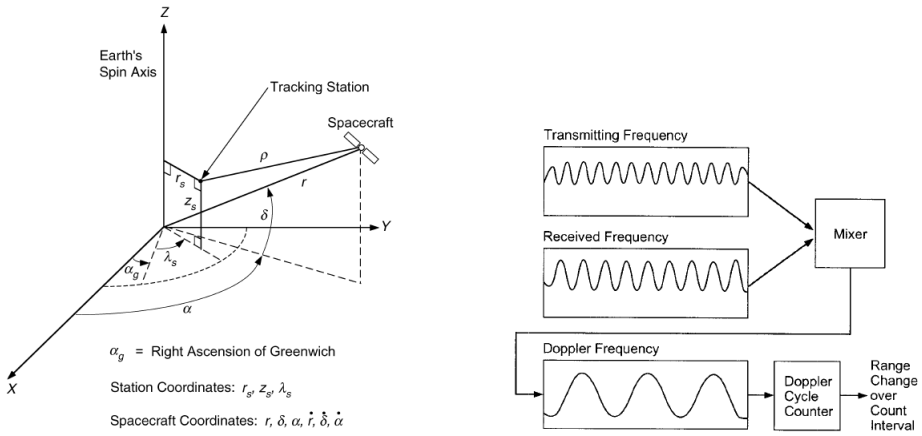

Figure 2.2. Left: s/c and stations coordinates. Right: simplified doppler observables process [12].

2.3.2 Very Long Baseline Interferometry

Very Long Baseline Interferometry, or VLBI, is at present the most accurate technique for measuring celestial angular positions at any wavelength, and the only method capable of milli-arcsecond precision for large number of objects. For example, it has been used in the past to accurately determine the positions of a large amount of quasars which were used to define the International Celestial Reference Frame (ICRF). The VLBI technique working principle is shown in figure 2.3 and described as follows.

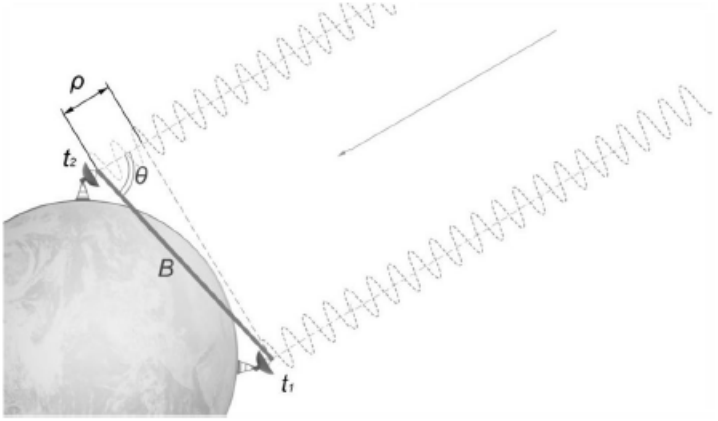

Figure 2.3. Basic concept of Very Long Baseline Interferometry [14].

An extra-galactic radio source emits electromagnetic waves that are received by two, or more, radio observatories. Being in different locations on Earth, the signal is received by the stations at different times. The time delay, τ, can be measured by amplifying, down-converting in frequency, and digitally sampling, the radiation received from the quasar at each antenna site with electronic processing devices. The radiation is perceived by the antennas as a planar wave front that propagates along the unit vector to the source, $\hat{s}_0$, and arrives at the two stations, which are separated by the so-called baseline vector $\vec{B}$ and point simultaneously at the same radio source. The time delay is then given by:

$$\tau_g = -\frac{\vec{B} \cdot \hat{s}_0}{c} = -\frac{B \cos\theta}{c} = t_2 - t_1 \tag{2.3}$$

where c is the speed of light and θ is the angle describing the geometric misalignment between the baseline and the direction of the incoming signal [15]. The determination of τ_g is performed through a cross-correlation process between the two signals that carry the sampled and digitalized quasar radiation. To derive the global delay τ, the process

requires to take also into account additional effects like Earth's rotation and atmosphere, clocks mis-synchronization, aberration, relativistic effects and efficiency of on-site devices. Moreover, we can highlight the sensitivity of the angle θ with respect to the time delay τ by differentiating the previous equation:

$$\frac{d\theta}{d\tau} = -\frac{c}{B\sin\theta} \tag{2.4}$$

From this result we can conclude that higher values of B translates into a lower sensitivity of θ with respect to errors in the measured τ [14], hence the need of ground antennas in different continents.
The same principles apply also to spacecrafts sufficiently far away from Earth. This technique can be effectively employed to track deep space missions, generating data sets that complement Doppler and range observations.

2.3.3 $\triangle$DOR observables

The Delta-Differential One Way Ranging, ΔDOR for short, is a specific application of differential VLBI to spacecraft tracking. Since VLBI measurements are affected by several error sources, it is possible to calibrate them by carrying out alternate DOR observations of the spacecraft and a nearby (in terms of angular position) quasar. The quasar will act as a calibrator, as its direction is typically known to better than 1 nrad, and a ΔDOR measurement can be formed by subtracting the quasar DOR from the spacecraft DOR. Generally, the observation sequence to construct a ΔDOR observation can either follow a s/c-quasar-s/c (S-Q-S) or a quasar-s/c-quasar (Q-S-Q) scheme. A single s/c-quasar (S-C) sequence is also acceptable. Since quasar and spacecraft VLBI measurements are taken with both antennas pointing to the same radio source, the single VLBI observations have to be performed at different times, in such a way that the observed values can

be interpolated. Generally, the time between two consecutive VLBI measurements is between 5-10 minutes [16].
The differential VLBI geometry is shown in figure 2.4. The direction to radio source 1 is indicated with $\hat{s}_1$ and the direction to radio source 2 is indicated with $\hat{s}_2$. The differential delay between source 1 and source 2 is given by:

$$\Delta\tau = \tau_1 - \tau_2 \approx -\frac{1}{c}\vec{B}\cdot(\hat{s}_1 - \hat{s}_2) \approx -\frac{1}{c}B\sin\theta_1(\theta_1 - \theta_2) = -\frac{1}{c}B\sin\theta_1(\Delta\theta_B) \tag{2.5}$$

where $\Delta\theta_B = \theta_1 - \theta_2$ is the component of the angular separation between the two radio sources in the direction of the baseline. Assuming 1 to be the spacecraft radio source, in the case of a S-Q-S sequence, τ_1, and consequently θ_1, derive from a linear interpolation of the respective values observed during the two spacecraft DOR. Finally, since a single ΔDOR observation gives us the position of the s/c along the baseline projection onto the plane-of-sky direction, to fully determine the angular position of the spacecraft, a second ΔDOR observation from a different baseline is needed.
This type of measurements are affected by different kind of errors which can be random or systematic. They are related to many factors, such as, for instance, the presence of the atmosphere, solar plasma, quasar positional uncertainties and clock instabilities. This topic will be addressed more in detail in Section 5.3.2, where we talk about the ΔDOR noise budget that we used to derive noise and uncertainties for the simulated ΔDOR observables.

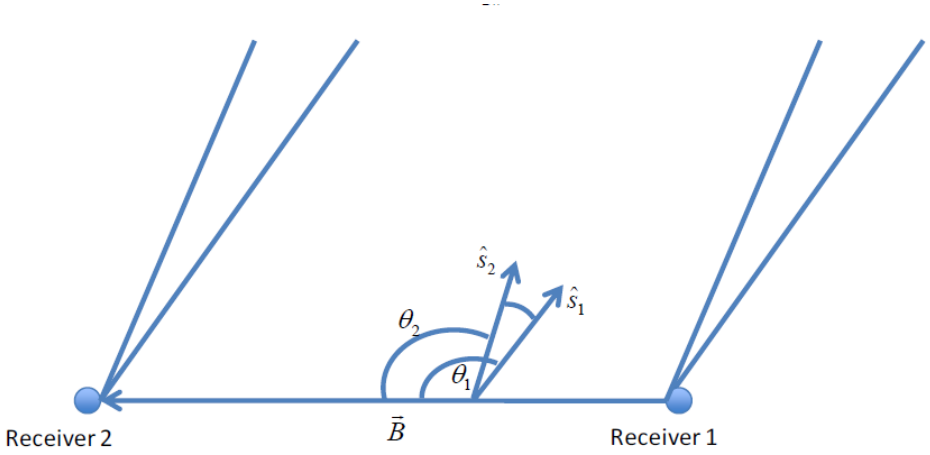

Figure 2.4. Differential VLBI geometry scheme [16].

2.4 Didymos data

The data used in the OD process is taken from the MPC online database. The MPC is the single worldwide location for receipt and distribution of positional measurements of minor planets, comets and outer irregular natural satellites of the major planets[2].
As of January 2024, 5599 optical observations of Didymos have been submitted by 165 different surveys from all over the world. Only 9 radar delay measurements have been reported, meaning that almost every measurement was obtained through optical techniques, which is a common trend in asteroid astrometry as highlighted by Chesley et. al. [17]. Moreover, no orbiting satellite measurements have been published for the Didymos system.
Figure 2.5 gives an overview over the years in which the measurements were performed. After a small peak in 2003, observatories began submitting large number of measurements only in recent times. From 2015 onward, the number of observations started becoming numerous

[2] `https://cgi.minorplanetcenter.net`

in preparation of the DART mission. The largest number of measurements were taken in 2022, when nearly half of the global observations were submitted.

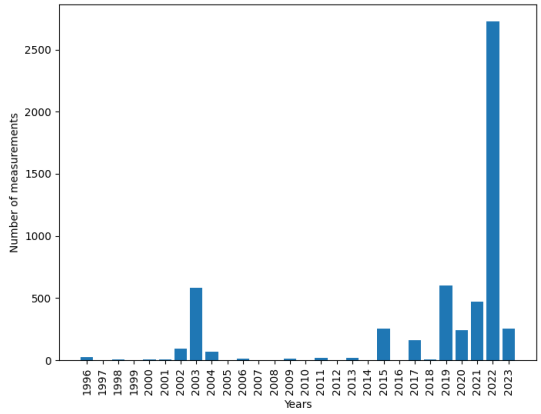

Figure 2.5. Number of Didymos optical measurements per year.

Figure 2.6 shows the catalogs employed in the observations of Didymos. For the sake of visualization clarity, the 12 star catalogs with a usage of less than 1% have been grouped together under the "Combined" label (table 2.2), while 67 submitted observations did not specify the catalog, hence the "Not specified" label. The catalogs belonging to the combined group are numerous but each of them has usage way below the GAIA ones (DR1, EDR2 and EDR3) which are by far the most employed. Together, they take more than 70% of the observations thanks to their large number of catalogued stars and levels of accuracy.

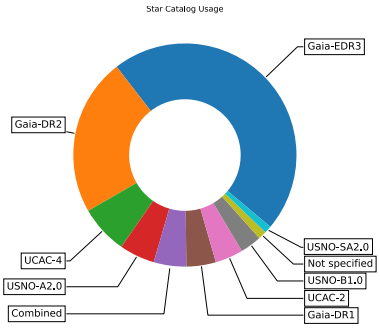

Figure 2.6. Star Catalogs usage

Star Catalog	No. Measurements	Percentage
Gaia-EDR3	2591	46,59%
Gaia-EDR2	1271	22,86%
UCAC-4	391	7,03%
USNO-A2.0	285	5,12%
Combined	263	4,73%
Gaia-DR1	237	4,26%
UCAC-2	225	4,05%
USNO-B1.0	172	3,09%
Not Specified	67	1,20%
USNO-SA2.0	59	1,06%

Table 2.2. Number of measurements and percentage usage of star catalogs

Figure 2.7 help visualize which ground stations contributed the most to the observations. Some surveys submitted a large number of observations in small time windows, others have been more consistent throughout the years, while the majority reported a few occasional observations. The upper plot of Figure 2.7 shows, from highest to lowest, the number of observations per station, with the Lowell Discovery Telescope (MPC code G37) being the single survey that submitted the largest number of observations, only second to the "Combined" group, which is introduced again for sake of visualization. The group collects 141 different stations that singularly make up for less than 1% of the global observations, but contribute together to approximately 30% of the total measurements. Considering only the optical observations, the telescopes used 11 different band-pass filters, represented on the MPC website by specific codes[3]. The second plot of the figure shows how many observations were taken in the respective band, with the red (R) filter being employed in more than 2500 times. Lastly, Table 4.2 presents the band-pass filters used by the surveys, the magnitude range of the observations and the star catalogs used with their percentage.

[3] `https://minorplanetcenter.net/iau/info/OpticalObs.html`

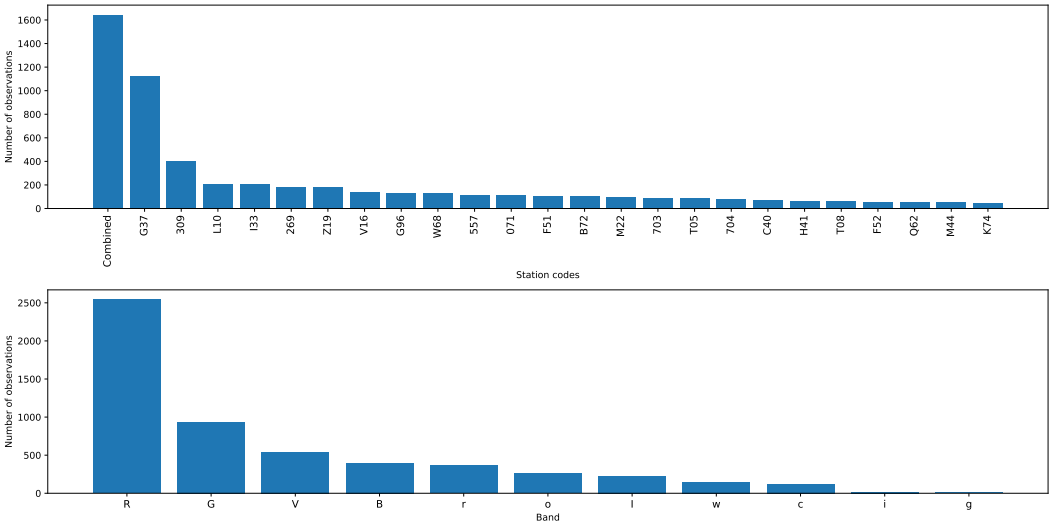

Figure 2.7. Number of observations per station (top) and band (bottom)

Table 2.3. Description of bands, observation magnitude range and catalogs used (with their percentage) for each survey.

Station code	**No. Mrs**	**Band**	**V**	**Catalog**	**Percentage**
G37	1123	G R	18,3-20,8	GAIA-DR2 GAIA-EDR3	0,62% 99,38%
309	404	R r	20,1-22,5	GAIA-EDR3 2:MASS	98,76% 1,24%
L10	209	I	16,1-17,9	GAIA-EDR3	100%
I33	204	R	18,3-18,8	GAIA-EDR3	100%
269	186	r	18,7-18,9	GAIA-EDR3	100%
Z19	181	R	19,2-19,6	GAIA-EDR3	100%
V16	138	G	13,0-17,9	GAIA-DR1	100%
G96	131	B V G	15,4-22,2	Not Specified UCAC-2 UCAC-4 GAIA-DR2	3,05% 18,32% 23,66% 54,96%
W68	129	c o	12,9-18,9	GAIA-DR2	100%

Station code	No. Mrs	Band	V	Catalog	Percentage
557	117	V r B	12,6-14,7	UCAC-5 GAIA-EDR3 UCAC-2	14,53% 27,35% 58,12%
071	114	R	13,0-15,4	USNO-B1,0	100%
F51	107	g r i w	16,0-22,3	GAIA-DR1 GAIA-DR2	10,28% 89,72%
B72	107	R G	13,6-19,3	GAIA-EDR3	100%
M22	97	c o	13,4-18,7	GAIA-DR2	100%
703	87	V B G	12,7-20,4	USNO-SA2,0 GAIA-DR2	1,15% 98,85%
T05	85	c 0	12,9-19,4	GAIA-DR2	100%
704	78	B	14,0-19,9	USNO-SA2,0	100%
C40	75	G	13,2-17,7	GAIA-DR2	100%
H41	66	R	11,8-17,8	USNO-SA2,0	100%
T08	61	o c	13,3-19,4	GAIA-DR2	100%
F52	59	i w	15,2-21,6	GAIA-DR2 GAIA-DR1	13,54% 86,44%
Q62	56	v r G	13,5-15,6	ATLAS-2 GAIA-DR2	14,29% 85,71
M44	53	V	13,6-14,7	ATLAS-2 UCAC-4	24,53% 75,47%
K74	50	G	13,7-17,7	Not Specified GAIA-EDR3 GAIA-DR2	12% 24% 64%

Finally, within the radar delay observations, we can distinguish two groups. The initial five observations, conducted in November 2003,

were carried by the Arecibo and Goldstone ground stations and corrected using the shape model published in Naidu et al. (2020) [18]. In contrast, the remaining four observations conducted between September and October 2022, were not corrected with the shape model resulting in larger residuals.

Chapter 3

Orbit determination in MONTE

MONTE is JPL's astrodynamic computing platform, supporting all phases of space mission development from early stage design and analysis through flight navigation. It is an interactive scripting environment that has access to the Monte C++ navigation and mission analysis libraries. From a capability perspective, the Monte software is designed to solve navigation and mission analysis problems. It can calculate and perform many of the common navigation tasks such as trajectories integration and targeting, Orbit Determination (OD), maneuver analysis.

In this work we use MONTE libraries to perform the OD and covariance analysis of the Didymos system. The OD process is an iterative estimation procedure based upon the comparison between the measured observables (real world data) and the corresponding computed values derived on the basis of mathematical models (simulated world). The differences between the observed and the computed observables are called residuals. The orbit determination solution is composed by the values of the solve-for parameters that minimizes, in a least square sense, the residuals, and by the corresponding covariance matrix that

defines the uncertainty of the solution. The OD process needs to be initiated by an a-priori estimation of the target's state and of the physical parameters. The trajectory of the body is propagated using an accurate dynamical model, which should include all relevant forces and perturbations acting on the system. The simulated trajectory gives the computed observables which are then compared to the corresponding real ones. In the ideal case, the residuals should match the measurement noise. However, in real world scenarios, dynamic and observation mis-modelling cause biases, drifts and discontinuities that have to be eliminated through the process of weighted least square linear estimation. Since dynamic and observation models are often non-linear, this procedure is repeated, using the previous estimated parameters as a-priori values for the new iteration, until convergence is reached [19]. The iterative procedure is presented in Figure 3.1.

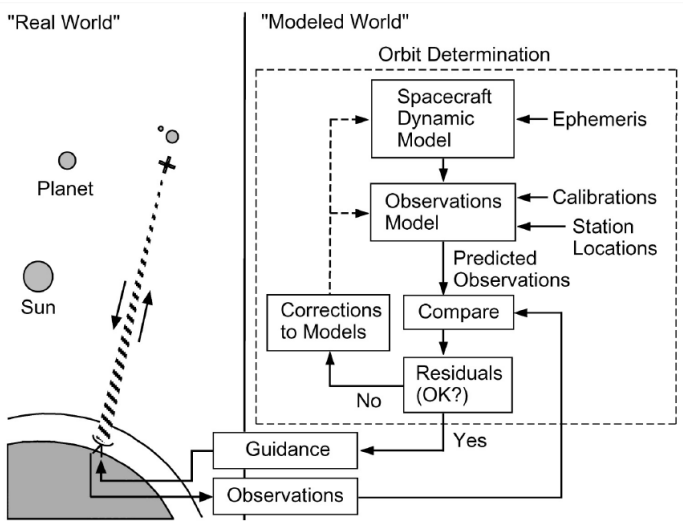

Figure 3.1. OD process flow diagram [19]

3.1 Dynamical model validation

The Monte environment allows to build a virtual universe by adding to the database the ephemerides and gravitational parameters of the Sun, planets, satellites and smaller bodies, whose gravitational interactions are handled by Monte thanks to its internal *Gravity* class. In addition to point mass gravity, relativistic corrections and relevant non-gravitational forces, such as the Yarkovsky effect, can be implemented into the model for higher fidelity simulations [20]. The dynamic model in our simulation set-up needs to be validated through the comparison between the integrated trajectory and a known solution for the Didymos system. In this case, we chose the JPL solution 181 because we had access to a detailed documentation describing its setup [21]. The solution delivers the ephemeris for the heliocentric orbit of the barycenter of the Didymos system, fitting 1041 optical measurements between April 1996 and February 2021 and 5 ground-based radar delay measurements. The next sections present more in-depth the dynamical model used for the JPL solution, which was then replicated in the Monte environment.

3.1.1 Didymos dynamical model

The primary forces acting on the asteroid come from the point-mass gravitational attractions of the Sun, the Moon, the planets and Pluto. The positions of these bodies are taken from the planetary ephemerides DE431. Other forces include the point-mass perturbations from the biggest 16 main-belt asteroids [22], whose positions and gravitational parameters are taken form the small bodies ephemerides sb431. Relativistic corrections are applied for the Sun, Moon and eight planets.
A non-gravitational acceleration induced by the Yarkovsky effect is also implemented into the model according to the formulation of Marsden and Yeomans [23]. This effect is due to the anisotropic emission of thermal radiation from a rotating body that is heated by the Sun. It

is modeled as a transverse acceleration of the form

$$a_t = A_2 r_n^{-d} \tag{3.1}$$

where A_2 is the acceleration magnitude at unit distance (estimated within the filter), r_n is the normalized heliocentric distance (normalizing factor $R_0 = 1$ AU), and the exponent d can vary between 0.5 and 3.5 [24]. In the case of Didymos $d = 2$ is taken. For solution 181, the A_2 *a posteriori* estimate is approximately $A_2 = -1.9 \times 10^{-14}$ au/d^2, which is the value used to replicate the solution.
The integration arc spans from 11-APR-1996 to 04-JUL-2024 with initial conditions given by the estimated orbital elements of the Didymos system in the 181 solution, which are listed in Table 3.1. Under these conditions, the comparison between the two trajectories yields a maximum deviation in terms of position and velocities of, respectively, 2.65 km and 0.48 mm/s. These differences could be related to the build-up, over the years, of numerical errors or discrepancies in the gravitational parameters of the asteroids. In any case, such a small difference over a large integration period was deemed to be small enough to consider the dynamical model validated.

Didymos state at epoch: 2015 Dec 23.50000 TDB				
Parameter	**Symbol**	**Value**	**Uncertainty**	**Unit**
Perihelion distance	q	1.01306233628123	4.911732E-09	AU
Semi-major axis	a	1.6442688825026	1.562112E-09	AU
Eccentricity	e	0.3838828022219	2.753811E-09	—
Inclination	i	3.40776816710425	1.327461E-06	°
Ascending nodes	Ω	73.22791476483350	9.669865E-06	°
Argument of perihelion	ω	319.233323014064	1.099674E-05	°
Perihelion passage time	T_p	183.40779	6.016286E-06	days
Period	P	2.1084332159124	3.029562E-09	years

Table 3.1. Estimated reference orbital elements for Didymos solution 181

3.2 Filter setup validation

Now that the dynamic of the system has been validated, the integrated trajectory can be passed through the real measurement of Didymos. In this way, the computed measurements can be compared to the real ones to obtain the residuals. If the observational model is correct, the derived Root Mean Square (RMS) values of the residuals are expected to be similar to the ones of the reference solution [21]. Using the navigation filter, it is then possible to derive an updated solution for the system. If the JPL solution falls inside the 3σ formal uncertainty range of the integrated one, the two can be considered statistically consistent. Therefore, the pre-processing schemes and filter parameters are likely to be correct and can be used for further OD analysis. The next section presents the schemes that were used to treat, *a priori*, the raw measurements.

3.2.1 Data pre-processing

The measurements pre-processing schemes we implemented are the ones described by Veres et al. [10] and Eggl et al. [25]. Veres describes a weighing scheme where measurements are grouped in batches. Consecutive observations from the same station, with a time gap smaller than 8 hours between each other, belong to the same batch. To take into account the correlation between measurements, if a batch has more than 4 observations, the associated weight is scaled by a factor of $\sqrt{N/4}$, where N is the number of observations in the batch. The weights depend mainly on the stations, many of which have fixed *a priori* values, while some may vary based on the epochs or the stellar catalogs used. For example, the Catalina Sky Survey, MPC code 703, has a sigma of 1.0" (for both Ra and Dec) if the observation was taken before 01-JAN-2014, 0.8" if it was taken after. This is done to account for hardware and software updates that improved (or degraded) the quality of the

observables over time.
Eggl describes a debiasing scheme to compensate for systematic errors found in star catalogs (Carpino et. al. [26]), derived from the analysis of Gaia's data. The scheme indicates that asteroid astrometric observations should be corrected by subtracting from the observed values the following quantities:

$$\Delta RA = \Delta RA_{2000} + \Delta\mu_{RA}(t - 2000.0)$$
$$\Delta DEC = \Delta DEC_{2000} + \Delta\mu_{DEC}(t - 2000.0)$$

where t is the observation epoch, ΔRA_{2000}, ΔDEC_{2000}, $\Delta\mu_{RA}$, and $\Delta\mu_{DEC}$ are tabulated quantities associated with each catalog needing corrections and the portion of the sky where the target is located. According to this scheme, the celestial sphere is divided into a certain number of tiles with the same surface area. Given the observed RA and Dec, we know which tile the observation belongs and we can derive the correction factors. Eggl describes two grids derived by dividing the celestial sphere using different number of tiles. In this work, we used the smoothed grid (higher number of tiles) to debias astrometric measurements.

Concerning the outliers, the rejection logic implemented in this work is based on a maximum value tolerable for the residuals. If the difference between a single residual and the mean value of the whole set is larger than a given threshold, the corresponding measurement will be ignored. The maximum value is taken as follows:

$$\xi_{max} = (1 + \frac{\Delta\sigma_F}{2})\sigma_F\sigma_\xi \tag{3.2}$$

where ξ_{max} is the residual threshold, σ_ξ is the standard deviation of the global set of residuals, σ_F and $\Delta\sigma_F$ are user-defined inputs input that allow to modify the threshold. In this case, a value of 3.5 was used for

σ_F and 0.15 for $\Delta\sigma_F$.
Regarding the radar measurements, the employed a *a priori* weights are the ones indicated on the Horizion[1] website page dedicated to Didymos.

3.2.2 Measurement residuals

The JPL 181 solution fits 1041 optical observations taken between April 1996 and February 2021 and 5 radar delay measurements, with 32 optical observations that have been rejected. In the solution presented in this work, 1043 observations were used, while 34 were rejected. This small difference comes from uncertainties in the pre-processing procedures used by the JPL. In the given observation arc, the number of measurements reported by the MPC is in fact way higher than the one reported by the JPL. Since no information in that regard was found, it was assumed that the raw data was binned every 2 minutes. The solution derived in this way, along with the dynamical model and the schemes presented in the previous sections, is quite close to the 181 solution. Figure 3.2 shows the derived right ascension and declination residuals. The RMS values are presented in Table 3.2, which also shows the comparison between the two solutions. Finally, the bottom plot of Figure 3.2 shows the weighted residuals, with most of them being inside the 1σ range.

[1] `https://ssd.jpl.nasa.gov/tools/sbdb_lookup.html#/?sstr=Didymos&view=OSPR`

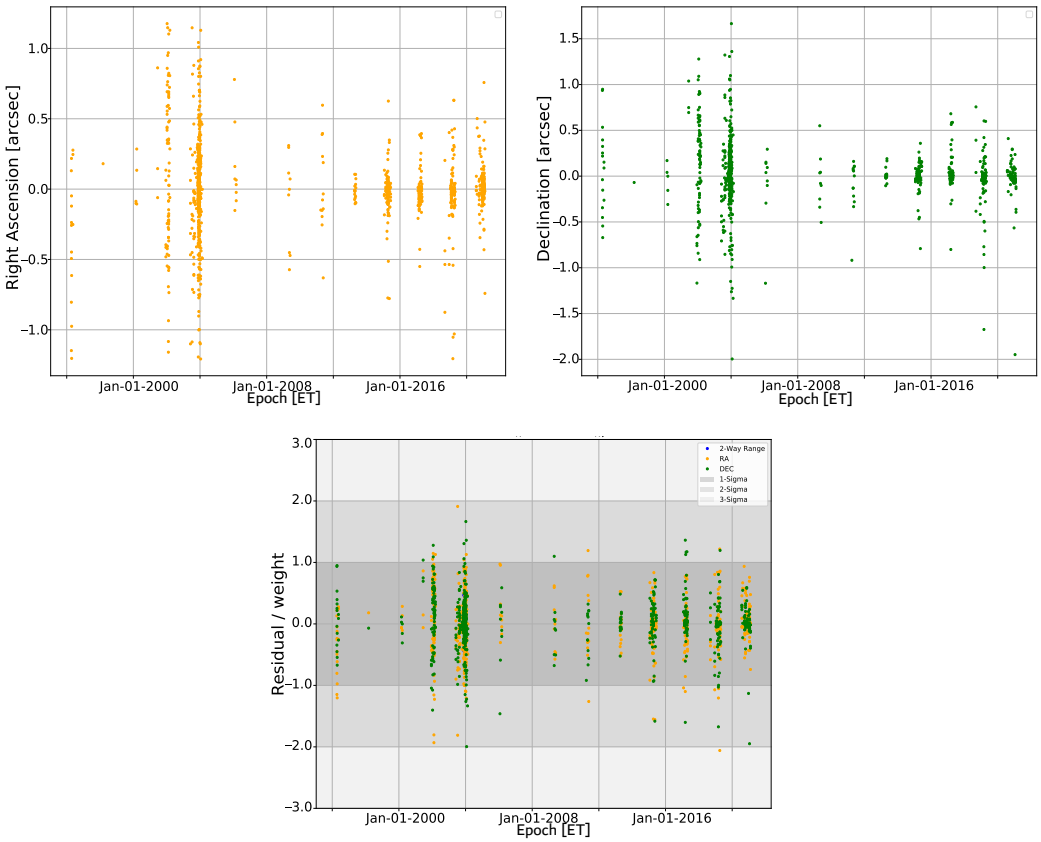

Figure 3.2. Right ascension (top left), declination (top right), and weighted (bottom) residuals as function of the epoch

3.2.3 Post fit solution and statistical validation

The filter solution with the corrected orbital elements is summarized in Table 3.2. From a comparison with the JPL 181 solution, we can see that the two are quite close, with parameters at reference epoch that are within a 0.5% difference.

Table 3.2. Comparison between the integrated and JPL 181 solutions

Optical residuals	JPL 181		Integrated solution	
No. optical observations	1041 used and 32 deleted		1043 used and 34 deleted	
	Ra	Dec	Ra	Dec
Mean weighted residuals	0.000	0.032	-0.005	0.022
RMS, unweighted (arcsec)	0.373	0.353	0.322	0.319
Radar Residuals				
No. delay observations	5 used and 0 deleted		5 used and 0 deleted	
	Delay		Delay	
Normalized RMS	0.302		0.309	
Corrected Orbital Elements (EMO2000) at epoch: 2015 Dec 23.50000 TDB				
	JPL 181		Integrated Solution	
Perihelion distance (AU)	1.01306233628123		1.00840986148772	
Semi-major axis (AU)	1.64426888250260		1.64426888745065	
Eccentricity	0.38388280222190		0.383882805387434	
Inclination (°)	3.40776816710425		3.40776413010168	
Ascending nodes (°)	73.22791476483350		73.2279138477404	
Argument of perihelion (°)	319.23332301406400		319.233321348063	
Perihelion passage time (days)	183.40779		183.40781	
Period (years)	2.10843321591240		2.10847016991328	

Figure 3.3 shows the variation in time of the position uncertainties with respect to the LOS (Line Of Sight) and RTN (Radial, Tangent, Normal) frames. The LOS frame, which is Earth-centered, has its first axis aligned with the orbit's normal direction, the third axis corresponds to the Earth-Didymos direction, and the second axis is determined by the cross product of the two. Conversely, the RTN frame is Sun-centered, with the primary axis defined by Didymos' radial direction, the third axis aligned with the orbit's normal direction, and the second axis given the cross product of the other two directions. A particular reduction in the uncertainties can be observed in correspondence of the radar observations, taken in November 2003. This behaviour is particularly evident in the LOS frame, where the uncertainty along the Earth-Didymos line of sight decreases to just 20 meters, as a result of the high information content along this direction and the m-level accuracy of radar delay observations. Figure 3.4 shows instead the position difference in the LOS and RTN frames between the JPL 181 solution and the filter so-

lution, which is taken as reference and therefore represented by the x-axis, while the blue areas represent the formal position covariances up to 3σ. We can notice that in the radial direction the difference grows with time. This is probably due to the lack of range measurements that constraint the position of Didymos, which is only given as result of the dynamic model implemented. Therefore, due to small discrepancies shown in section 3.1.1, the difference is growing. Another notable aspect is the constant drift in the tangential direction. This behaviour is probably due to the Yarkovsky effect, which was modelled as a non-gravitational acceleration acting only in the tangential direction. Nonetheless, the JPL 181 solution falls within the 3σ range, indicating that the integrated solution can be considered statistically equivalent to the reference one.

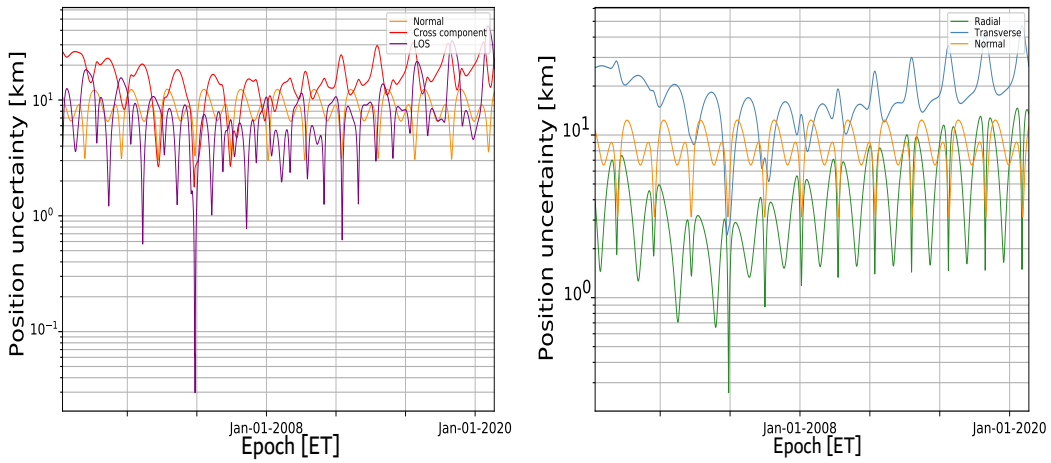

Figure 3.3. Didymos barycenter position uncertainties variation in time with respect to the LOS (left) and RTN (right) frames.

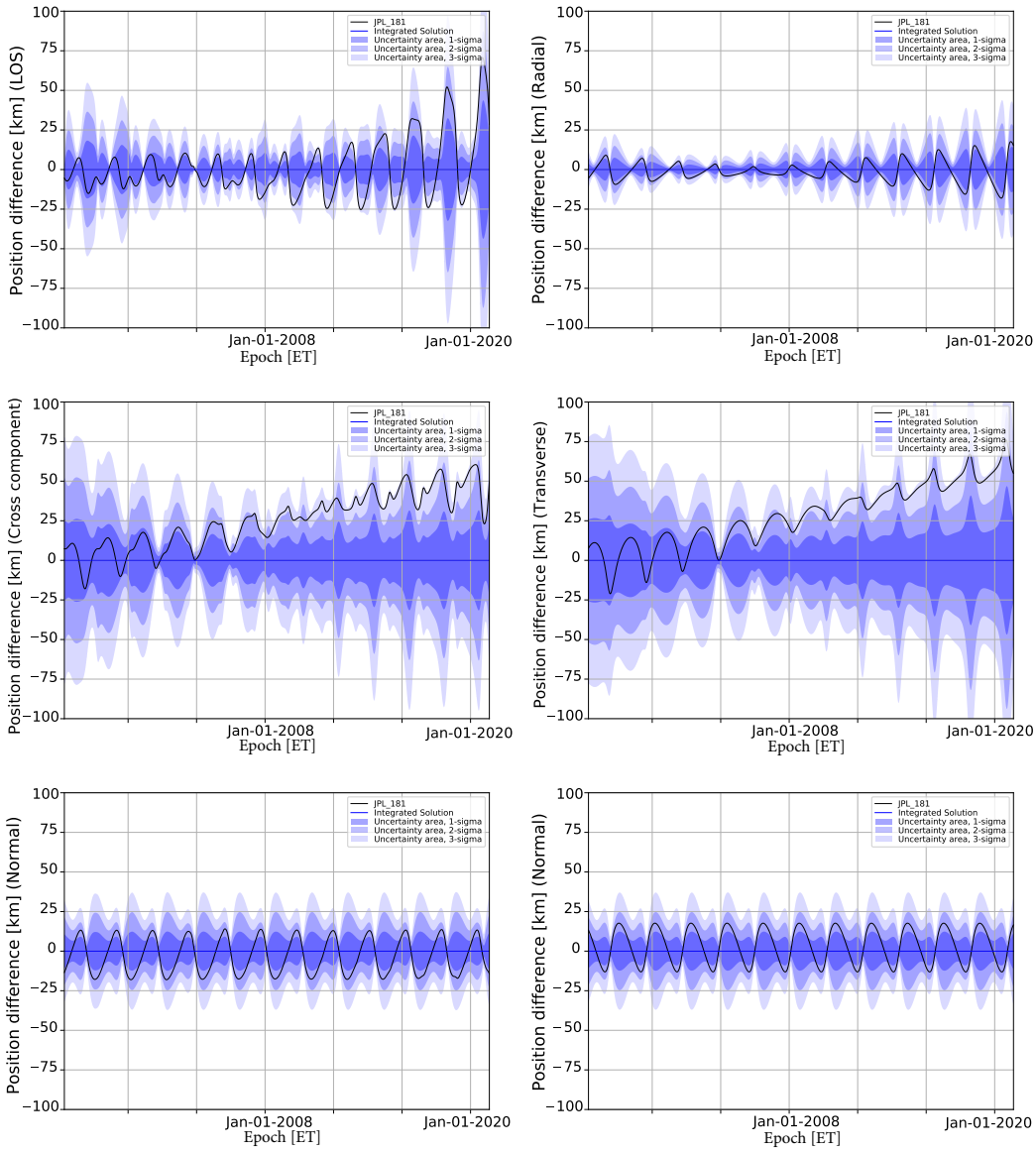

Figure 3.4. Didymos barycenter position differences between estimated solution and the reference JPL solution with respect to the LOS (left column) and RTN (right column) frames.

Chapter 4

Reference solution

With the complete model now validated we can proceed with our analysis. In this section we give an overview on the procedure that we followed, which is summarized in Figure 4.1 and discussed as follows.

1. We start by introducing the dynamical model, dataset and initial conditions used to match the publicly available data at the time of the present study, and the most recent orbital solutions.

2. We analyze the astrometric and radar data available in the Minor Planet Center (MPC), comment on the estimated ephemeris solution, and draw some initial conclusions on the measurability of $\beta_\odot$ and A_2.

3. Using as *a priori* condition the derived reference solution, we propagate the trajectory forward in time and simulate future astrometric data, and pseudo-range and ΔDOR measurements that will be collected by the Hera mission.

4. We establish various observation scenarios by selecting sub-groups of observations from the global dataset derived from the measurements simulation, and we perform the OD process for all cases to

obtain a set of solutions.

5. We analyze the results and compare the various measurement contributions to the uncertainty reduction, focusing mainly on the measurability of $\beta_\odot$ and A_2 and their correlation.

6. Finally, we perform a sensitivity analysis to assess how the number of simulated observations influences the results. Specifically, we address the influence of the baseline selection and frequency of ΔDOR measurements on the solution's covariance.

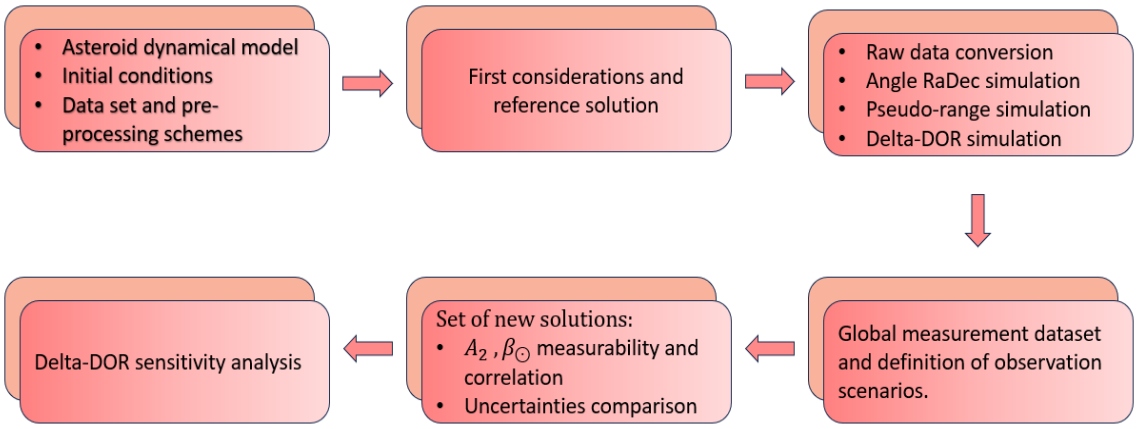

Figure 4.1. Analysis procedure scheme.

The next sections and chapters will expand on the points presented here, starting from the new model implemented.

4.1 Updated dynamical and observation model

In this analysis we implemented a slightly different dynamical model from the one described in the previous chapter to include the $\Delta\vec{v}$ pro-

vided by DART's impact, and the latest planetary ephemerides file. The new dynamic of the system is therefore determined by:

- Point mass gravitational attraction from the Sun, the Moon, 8 planets and Pluto, with relativistic correction applied for all except Pluto (ephemeris file DE440).
- Point mass perturbation from the 16 biggest asteroids of the main asteroid belt (ephemeris file sb441).
- Yarkowsky effect according to the Marsden and Yeomans model. We use the same formulation and values presented in section 3.1.1.
- The momentum variation of the Didymos' system barycenter can be expressed as in Equation (1.3). By rearranging the expression we get:

$$\Delta\vec{v} = \beta_{\odot}\frac{\vec{p}_{DART}}{M_{sys}} \tag{4.1}$$

  where $\vec{p}_{DART}$ is DART's relative momentum at the impact epoch and M_{sys} is the mass of the system. This formulation holds if we assume the $\Delta\vec{v}$ to be impulsive and in the direction of DART's relative velocity, and all of the ejecta is escaping the system instantaneously and in opposite direction to $\vec{p}_{DART}$. All of the vectors are expressed in the EME2000 frame.

The mass of the system is shown in table 1.1, while the values associated to DART's relative velocity and mass are taken from Daly et al. [27] and from the spice kernels for the DART mission[1]. The most important parameters needed to model the $\Delta\vec{v}$ are reported in the following table.

[1] `https://naif.jpl.nasa.gov/pub/naif/pds/pds4/dart/dart_spice/`

Parameter	Value	Unit
M_{sys}	5.6×10^{11}	kg
M_{dart}	579.4	kg
v_x	3.573	km/s
v_y	-4.642	km/s
v_z	-1.856	km/s

Table 4.1. Most relevant parameters for $\Delta\vec{v}$ computation.

In this solution we fit all of the data available for the Didymos system as of January 2024, which we presented in section 2.4 and summarized here in Table 4.2. The 9 radar delay measurements are modelled in Monte as two-way range observations. The pre-processing schemes are the ones described in section 3.2.1.

Msr No.	Type	First point (TAI)	Last point (TAI)
9	Radar Delay	14-NOV-2003 09:00:32	08-OCT-2022 12:50:37
3891	Pre-Impact Angle Ra-Dec	11-APR-1996 06:42:33	26-SEP-2022 23:15:00
1708	Post-Impact Angle Ra-Dec	26-SEP-2022 23:17:30	12-JUN-2023 06:12:50
5608		11-APR-1996 06:42:33	12-JUN-2023 06:12:50

Table 4.2. Available measurements for Didymos on the MPC.

4.2 Initial conditions and filter set-up

We perform a single arc estimation with initial epoch on 11-APR-1996 and final epoch now set on 25-JUL-2027 (end of Hera mission). The set of solve-for parameter includes the state of the Didymos system expressed in Cartesian coordinates, A_2 and the magnitude ΔV of the velocity variation vector. We can then use Equation (4.1) to derive $\beta_\odot$ and its uncertainty from the filter solution. For consistency reasons, the initial conditions are the same as the ones presented during

the model validation in the previous chapter, with the addition of the initial value for the ΔV. This value is derived by substituting the quantities reported in Table 4.1 into Equation (4.1), and assuming as initial guess $\beta_{\odot} = 3$. This assumption was made on the basis of ejecta particle simulation and the measured value of the β parameter. Numerical simulations performed by Makadia et al. [7] showed that 88% of Dimorphos's ejecta particles are expected to have escaped the system's gravitational attraction, along with as 95% of DART's spacecraft mass. We already showed in Chapter 1 that a value of β of $3.61^{+0.19}_{-0.25}$ has been estimated for Dimorphos' momentum enhancement. Therefore, $\beta_{\odot} = 3$ seems a plausible assumption since not all of the ejecta have escaped the system.
The updated initial conditions are reported in Table 4.3, while the filter set-up is summarized in Table 4.4. We specify that we solve for Didymos' state in Cartesian coordinates because of MONTE's filter formulation, which does not allow to directly estimate the state in terms of conical coordinates.

Ref epoch: 23-DEC-2015 12:00:00 ET		
Parameter	*A priori* Value	Unit
a	1.644268883	au
e	0.383882802	—
i	3.407768167	deg
Ω	73.22791476	deg
ω	319.233323	deg
T_p	183.40779	days
A_2	$-1.88583951517 \times 10^{-14}$	au/day^2
ΔV	$1.90731874732 \times 10^{-8}$	km/s

Table 4.3. Integration initial conditions.

Solve-for-parameter	*A priori* covariance	Unit
x	100	km
y	100	km
z	100	km
dx	1.00×10^{-5}	km/s
dy	1.00×10^{-5}	km/s
dz	1.00×10^{-5}	km/s
A_2	7.226558×10^{-15}	au/day^2
ΔV	1.00×10^{-7}	km/s

Table 4.4. Solve-for-parameters with *a priori* uncertainties.

4.3 Solution covariance and parameters estimation

With the set-up discussed in the previous sections, the estimation process yields the following results for our parameters of interest, A_2 and $\beta_\odot$:

- $A_2 = -1.846 \times 10^{-14} \pm 6.92 \times 10^{-15}$ au/day^2 (1σ), which implies a signal-to-noise ratio SNR= 2.669.
- $\beta_\odot = 3.128 \pm 15.719$ (1σ), corresponding to SNR= 0.199.

While the filter is able to give a good estimate for A_2, this is not the case for $\beta_\odot$ since its uncertainty is much larger than the estimated value, resulting in very low SNR. Therefore, we conclude that current observations are insufficient to give an accurate estimate for $\beta_\odot$, and the post-impact heliocentric orbit of the system derived in this way is not statistically valid. For this reason, instead of focusing on the actual value of the solve-for-parameters, we perform in the following sections a covariance analysis to determine the formal uncertainty (and corre-

sponding SNR value) of A_2 and $\beta_\odot$ under different future observation scenarios. This will allow us to determine the expected performances of future OD processes that will be performed when the actual observation of Hera and Didymos will be available.
To perform this analysis, we need to choose a trajectory and consider it as the "truth" since it will be the reference for the measurements simulation. Said trajectory was derived with the same set-up described in this section, assuming $\beta_\odot = 3$ as the truth. Under this assumption, we obtain an *a posteriori* value for A_2 of -1.739×10^{-14} au/day^2, which will be used in Chapter 6 and 7 to compute the signal-to-noise ratios.

Chapter 5

Measurement simulation

This chapter is dedicated to addressing how we derived synthetic tracking data for Didymos and the Hera s/c, and the relative noise models and weighing schemes.
First, we chose to convert the real observations of the system into synthetic observations by converting the corresponding computed measurements. This was done because past observed measurements are based on the "real world" dynamics, which is extremely complex and different from our "modelled world". Through this conversion we ensure that past and future observations both refer to the same model, adopting a more rigorous approach.
In this work we simulated astrometric angular measurements of the asteroid, range and ΔDOR observations of Hera. The presence of an orbiting spacecraft around the asteroid system allows us to correlate spacecrft tracking observations to asteroid position measurements, and derive meter-level constraints on the distance between the Earth and Didymos. These kind of range observations, called pseudo-range measurements, have already been used in past missions to reconstruct the ephemerides of celestial bodies visited by spacecrafts, and have shown great performance for orbit determination accuracy [28] [29].

5.1 Astrometric observables

Predicting when and how ground telescopes will observe Didymos is quite difficult. However, we can make good assumptions based on past observations and analytical formulations that we can use to predict when the asteroid will be visible from a station. The procedure followed for the simulation of astrometric observables is summarized in figure 5.1 and described as follows.
We first selected 11 stations among the 20 surveys that submitted the largest amount of astrometric observations to the MPC. The selection was primarily based on the telescopes' capacity to detect faint objects. This characteristic was assessed either by looking at past data or from the telescope specifications. For each of the chosen stations, a series of photometric and geometric conditions have to be satisfied for the asteroid to be visible. If these conditions are met, we can derive a list of time windows in which we know that the station can observe the asteroid, thus creating a global observability window pool. To obtain a realistic number of measurements, we then randomly draw a given number $N = r\Delta t$ of station-specific intervals from the window pool, where r is the data rate (number of observations per year) during periods of similar visibility conditions, and Δt is the simulation time span (from January 2024 to July 2027). Knowing the time window and the corresponding station performing the measurement, we derive the celestial coordinates of Didymos from its reference trajectory at the epoch of maximum elevation (as seen from the observer). Finally, we add Gaussian noise to obtain the synthetic astrometric observable.

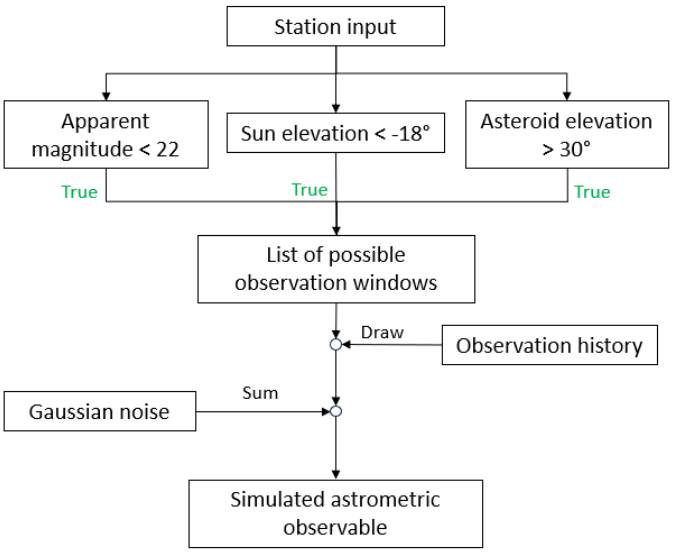

Figure 5.1. Astrometric observables simulation scheme.

The first condition represented in figure 5.1 indicates the necessity for the asteroid to be bright enough to be visible from ground telescopes. In astronomy, the measure of the brightness of an object is called magnitude, which is a unit-less quantity defined on a logarithmic scale. The brighter an object appears, the lower the value of its magnitude. We call apparent magnitude (V) the magnitude of an asteroid when observed and measured visually or with a CCD camera. We instead call absolute magnitude (H) the magnitude of an asteroid at a distance of 1 AU from the Earth and 1 AU from the Sun with null phase angle (Sun-Asteroid-Earth angle, α). In our analysis, we have taken $V = 22$ as a threshold value beyond which Didymos was considered to be not bright enough. This value comes from telescope specifications and past observations, where very few cases have shown V values greater than 22.

To determine if the asteroid will be visible in the near future, we need to predict its apparent magnitude. There exists analytical formulas that

correlate H, V, α and some physical properties of the asteroid [30], also known as the H-G magnitude system.

$$H = H(\alpha) + 2.5 \log (1 - G)\phi_1(\alpha) + G\phi_2(\alpha) \tag{5.1}$$

$$H(\alpha) = V - 5 \log(r\Delta) \tag{5.2}$$

where:

- r is the asteroid's heliocentric distance
- Δ is the asteroid's geocentric distance
- H(α) is the reduced magnitude, i.e. the magnitude value assuming that the asteroid is 1 AU from both the Sun and the Earth
- G is the slope parameter
- $\phi_i(\alpha) = \exp\{-A_i[\tan(\frac{1}{2}\alpha)]^{B_i}\} \quad i = 1, 2$

with $A_1 = 3.33$, $A_2 = 1.87$, $B_1 = 0.63$ and $B_2 = 1.22$. Knowing the trajectory of the system, we can derive r, Δ, and α, while $G = 0.2$ and $H = 18.16$ are taken from previous investigations from literature [4]. From equations (5.1) and (5.2) we can derive V, which represents the expected apparent magnitude and is plotted against time in the top plot of Figure 5.2. The black dots indicate the values of V reported in the MPC for past observations, which are used for validation of the computed values for future measurements. For the same purpose, the bottom plot shows the apparent magnitude residuals (expected minus observed). The residuals, which show almost zero mean and RMS = 0.42, are small enough to consider the model validated.

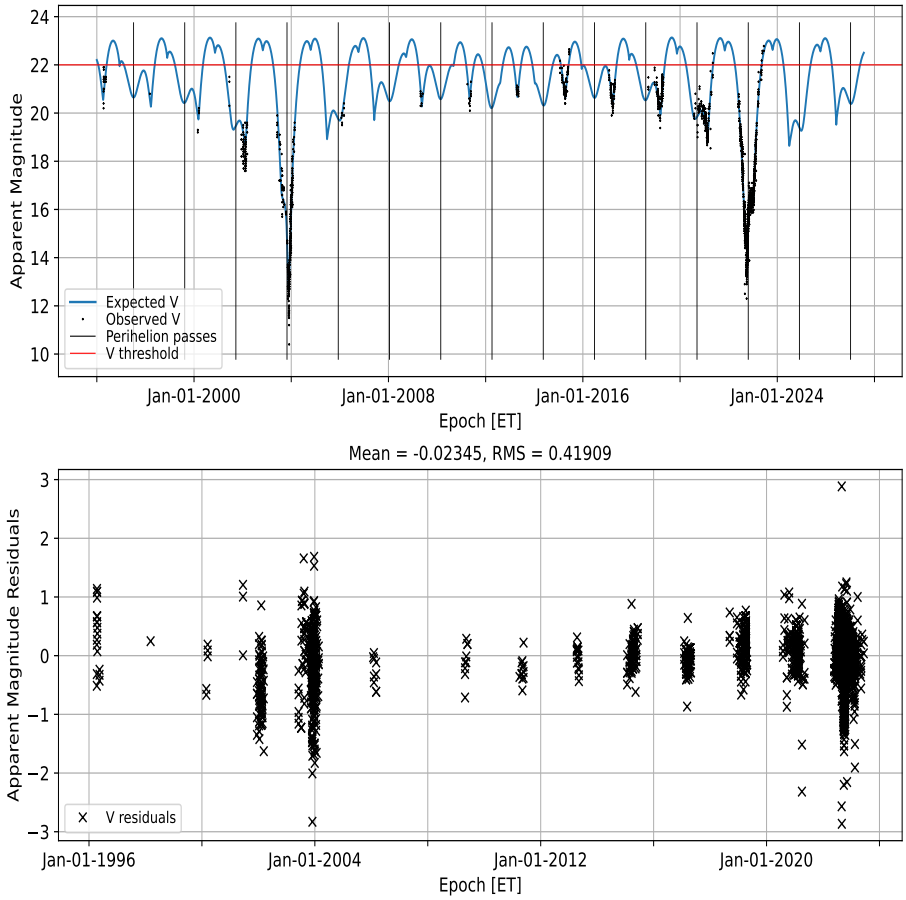

Figure 5.2. Top: Computed (blue line) and observed (black dots) values of the apparent magnitude of Didymos as a function of time; bottom: apparent magnitude residuals

The second condition in Figure 5.1 indicates that the Sun needs to be below the horizon with an angle greater than 18°. This is a recommended practice to avoid twilight effects that could make it more difficult to observe fainter objects.
The last condition indicates that the asteroid should have an elevation greater than 30° with respect to the observer. This is another recom-

mended practice suggested by the MPC to avoid airmass disturbances[1]

5.2 Pseudorange observables

Radiometric observables have been generated assuming the availability of ESA's tracking stations network (ESTRACK), which includes deep space antennas at Cebreros (CEBR), New Norcia (NNOR), and Malargüe (MGUE).
Hera will carry an X-band transponder and will be in communication with ground stations for the whole duration of the mission. We therefore simulated two-way range measurements at X-band for every nominal phase of the mission. Each range observation is computed for the ground station that sees Hera with the highest elevation in uplink and downlink, while also assuring a minimum elevation of 5°.
The noise added to the i-th range observable, corresponding to the weight used within the OD filter, is the result of three contributions which are combined to derive the total noise σ_i:

$$\sigma_i = \sqrt{\sigma_{range}^2 + \sigma_{bias}^2 + \sigma_{rel}^2} \tag{5.3}$$

where $\sigma_{range} = 0.5$ m [31] is the typical uncertainty associated with X-band range measurements, $\sigma_{bias} = 3$ m is a conservative assumption for the range bias noise contribution. The last term is related to the accuracy of Hera's relative orbit with respect to Didymos, which is used to map the range measurements from the probe to its small body target. Gramigna et al. [31] computed the variation of the mutual orbit uncertainties for the whole duration of the mission. Expressing the uncertainties in the Earth RTN frame we find the radial component of σ_{rel}, which we show on a logarithmic scale in Figure 5.3, to vary between 10^{-2} and 10^{-3} km, making it the biggest uncertainty contribution for

[1] `https://www.minorplanet.info/php/photometryguide.php`

most of the simulated observations. For now, we are not interested in the other directions since we are processing range observables.
Given the epoch of the i-th measurement, we derive the associated relative uncertainty and we substitute its value in Equation 5.3 to derive the noise and weight to assign to the i-th measurement. For the covariance analysis presented in this work we use one range measurement per Hera OD arc [31], taken in correspondence of the local point of minimum of the mutual orbit uncertainty.

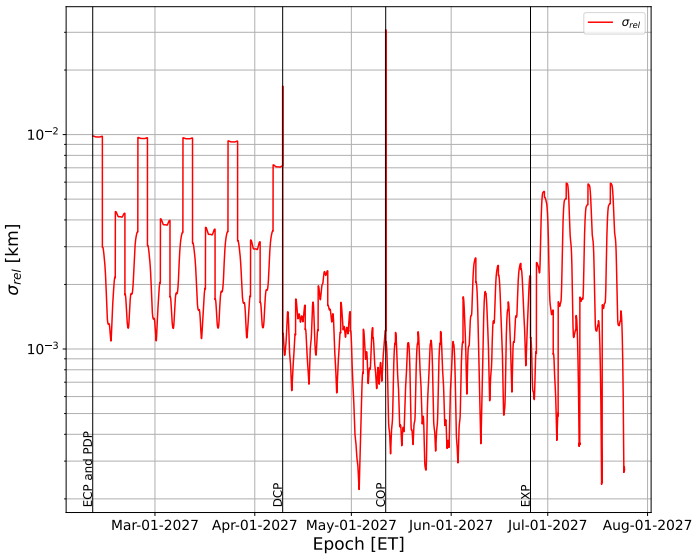

Figure 5.3. Variation of the radial component of the mutual orbit uncertainty in the Earth RTN frame as a function of time. The vertical lines represent the beginning of the nominal mission phases.

5.3 ΔDOR observables

We simulated ΔDOR measurements for the three baselines determined by the ESTRACK stations, following a similar procedure to the one described for the range observables. We derived a series of tracking

passes for each pair of stations, with the only condition that Hera must be seen from both stations with an elevation greater than 10°. Figure 5.4 shows the time variation of Hera's elevation angle with respect to the ground stations for the first days of the ECP. Similar geometries are also observed during the rest of the proximity phases, which are not depicted in the Figure for the sake of readability.
The Figure demonstrates that there is no coverage for the MGUE-NNOR baseline, since the visibility condition is never satisfied. Moreover, the plot shows that the CEBR-MGUE and CEBR-NNOR baselines have a time window of roughly 5 and 3 hours respectively, during which ΔDOR measurements can be collected. Finally, the mean elevation observed with the two baselines results to be different. This will influence the ΔDOR error budget, as we will show later in Section 5.3.2.
Given these considerations, we only simulated ΔDOR observations for the CEBR-NNOR and CEBR-MGUE baselines.

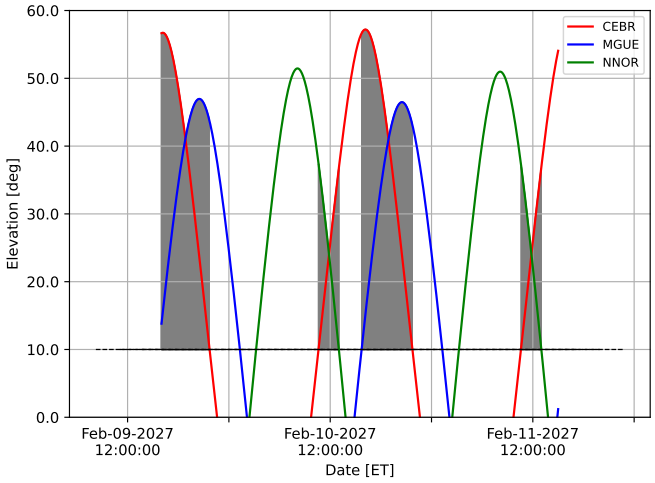

Figure 5.4. Hera's elevation angle with respect to the ESTRACK ground stations. The gray areas represent the time interval during which two stations see Hera with an elevation greater than 10°.

ΔDOR measurements are computed internally by MONTE from an input sequence of VLBI measurements, following a spacecraft-quasar-spacecraft (S-Q-S) scheme [16], where each measurement is computed 8 minutes apart from each other. The epoch for the quasar VLBI is taken in correspondence of the middle point of the passes' time interval, which also becomes the epoch for the ΔDOR observation. The epochs for the two spacecraft VLBI are derived by summing and subtracting 8 minutes from the observation epoch. From the S-Q-S sequence MONTE linearly interpolates all of the quantities associated to the spacecraft VLBI measurements to construct a single VLBI measurement, which is subtracted to the quasar VLBI to generate the ΔDOR observable.
We conducted simulations involving three VLBI sessions per day for each baseline, generating one ΔDOR per day for both the CEBR-NNOR and CEBR-MGUE baselines. It's worth noting that this represents an extreme scenario, given the considerable costs associated with VLBI operations. For this reason, in our covariance analysis we consider a reference of 3 measurements per baseline for the whole mission. In Chapter 7, we also delve into a sensitivity analysis to evaluate the anticipated OD performances by varying the number of ΔDOR observations.

5.3.1 Quasar selection

To generate ΔDOR measurements, a quasar needs to be defined for each S-Q-S sequence. When planning ΔDOR support for a mission, there is often a trade-off in the choice of the quasar to minimize noise [32]. Generally, errors are smaller for stronger sources at smaller spacecraft-quasar angular separation. However, a quasar at a larger angular distance may be less noisy than a weaker, but closer, source. Additionally, the characterization of the flux received by baselines from different quasars has only been carried out for selected sources and DSN[2] sta-

[2]Deep Space Network: NASA's network of deep-space antennas

tions. Prior to the Hera mission, dedicated campaigns should be conducted to thoroughly characterize quasar fluxes and precisely evaluate the error budget for the ESTRACK baselines. To simplify our analysis we focused mainly on the angular separation, and we defined a priori a set of X-band quasars at minimum angular distance from the reference trajectory. Given that we simulate one ΔDOR per day, each day of the mission will then be associated to a quasar at minimum angular separation from Hera.
Figure 5.5 shows Hera's celestial coordinates with respect to the Earth in the EME2000 frame, and the quasars populating the given portion of the sky, represented by a black cross. The red crosses indicate the selected quasars, whose names are also reported. The quasars' position are taken from the X-band radio source catalog [33].

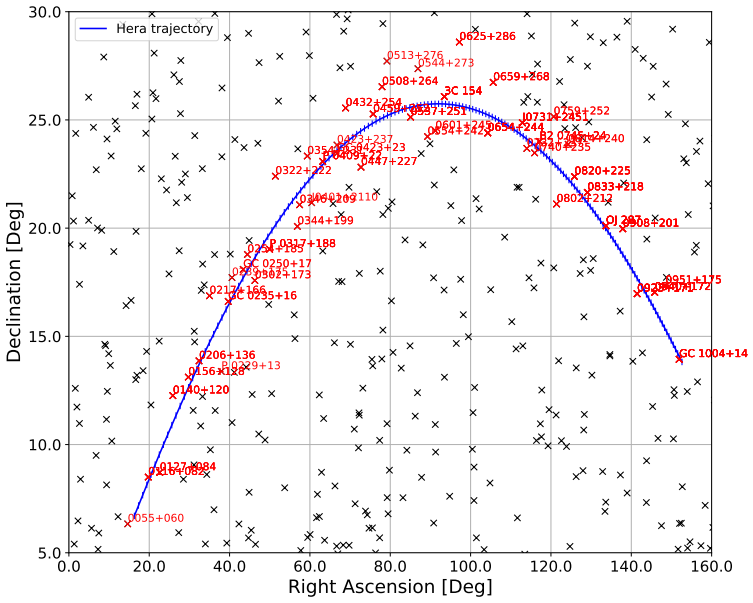

Figure 5.5. Hera and quasars celestial coordinates in EME2000 and center on Earth.

5.3.2 △DOR noise budget

The ΔDOR error budget depends on many factors including, for instance, observation geometry, clock instability, solar plasma, and atmospheric disturbances. The different contributions, which can be systematic or random, are then root-sum-squared to obtain the global error. The equations used to derive each contribution are listed in the CCSDS technical report [16], where it is also shown the error budget for a typical X-band NASA case. Some of the quantities appearing in the equations are taken from the general case, while quantities related to the geometry of the single observation (for example, spacecraft and quasar elevation) are computed for each measurement. We specify that the angular separation used in the evaluation of the noise budget is not the one computed for the selected quasar, but is instead fixed at $\Delta\theta = 5°$, which is the typical value listed in the CCSDS report. This choice was made because the computed angular separation resulted to be quite low, thus affecting the error budget. Given that the selection of the quasars will be made in the future by ESA's Flight Dynamics team, we decided to adopt a conservative approach by assuming a larger and fixed angular separation, which will yield higher noises and uncertainties.
The analytical equations describing the error contributions are listed below (refer to [16] for a detailed description of the individual terms appearing in the equations and the assumptions made in their derivation):

1. Quasar thermal noise (random)

$$\sigma_{qu} = \frac{\sqrt{2}}{2\pi f_{BW}} \frac{1}{SNR_{qu}} \tag{5.4}$$

with SNR_{qu} given by:

$$SNR_{qu} = K_L \frac{10^{-26}}{2k} \frac{\lambda^2}{4\pi} S_c \sqrt{(G/T)_1 (G/T)_2} \sqrt{DT_{qu}} \tag{5.5}$$

2. Spacecraft thermal noise (random)

$$\sigma_{sc} = \left[\left(\frac{\sqrt{2}}{2\pi f_{BW}} \frac{1}{SNR_{sc_1}} \right)^2 + \left(\frac{\sqrt{2}}{2\pi f_{BW}} \frac{1}{SNR_{sc_2}} \right)^2 \right]^{1/2} \tag{5.6}$$

with the s/c SNR and signal-to-noise spectral density for the k-th station of the baseline given by:

$$(P_{DOR}/N_0)_k = P_{tran} \left(\frac{\lambda}{4\pi R} \right)^2 \frac{1}{k} (G/T)_i \tag{5.7}$$

$$SNR_{sc_k} = \sqrt{2(P_{DOR}/N_0)_k T_{sc}} \tag{5.8}$$

3. Clock instability (random)

$$\sigma_{clock} = T_{sc\_qu} \sigma_{\Delta f/f} \tag{5.9}$$

4. Disperisve phase (random)

$$\sigma_{phase} = \sqrt{2}\sqrt{2} \frac{\sigma_\Phi}{360} \frac{1}{f_{BW}} \tag{5.10}$$

5. Station location (systematic)

$$\sigma_{stn} = \frac{1}{c} (\Delta\theta) \sigma_{BL} \tag{5.11}$$

6. Earth orientation (systematic)

$$\sigma_{stn} = \frac{1}{c} (\Delta\theta) \sigma_{UTPM} \tag{5.12}$$

7. Zenith troposphere (systematic)

$$\sigma_{tropo} = \frac{\rho_z}{c} \left| \frac{1}{\sin\gamma_{sc} + 0.015} - \frac{1}{\sin\gamma_{qu} + 0.015} \right| \tag{5.13}$$

with ρ_z representing the wet ($\rho_{z_{wet}}$) or dry ($\rho_{z_{dry}}$) troposphere delay uncertainty at each station. This results in 4 terms that need to be root-sum-squared to obtain zenith troposphere contribution.

8. Fluctuating troposphere (random)

$$\sigma_{tropo_{fluct}} = \frac{1}{c}\frac{\Delta\theta}{0.1745}\rho_{tropo_{fluct}} \tag{5.14}$$

9. Ionosphere shell (systematic)

$$\sigma_{iono} = 0.02 \times 10^{-9} \tag{5.15}$$

10. Fluctuating ionosphere (random)

$$\sigma_{iono_{fluct}} = \frac{1}{c}\frac{\Delta\theta}{0.1745}\rho_{iono_{fluct}} \tag{5.16}$$

11. Solar plasma (random)

$$\sigma_{plasma} = \frac{0.013}{f_{RF}^2}[\sin SEP]^{-1.3}\left(\frac{B_s}{v_{SW}}\right)^{0.75} \times 10^{-9} \tag{5.17}$$

12. Quasar coordinate (systematic)

$$\sigma_{qu_{coord}} = \frac{B_p}{c}\sigma_\theta \tag{5.18}$$

Note that all the equations yield σ values expressed in seconds. The error may be converted from units of time delay to units of angle by multiplying by the speed of light and dividing by the length of the baseline projected onto the plane-of-the-sky. The angular error may then be converted into a position error at the spacecraft, normal to the line of sight, by multiplying for the Earth-spacecraft distance.
The 12 error contribution are root-sum-squared to obtain the noise $\sigma_{RSS,i}$ associated to the i-th measurement:

$$\sigma_{RSS,i} = \sqrt{\sum_{j=1}^{12}\sigma_{i,j}} \tag{5.19}$$

5.3.3 $\triangle$DOR measurement uncertainty

Just like we did for the pseudo-range, when weighting the measurements we need to take into account also the uncertainty component related to Hera-Didymos mutual orbit. In this case we need to rotate the uncertainty vector along the direction of the baseline projection onto the plane-of-sky. For this purpose, for each measurement we define a frame of reference on the baseline with first axis $\hat{B}_\perp$ along the baseline projection, third axis along the spacecraft line of sight $\hat{R}$, and second axis $\hat{y}$ given by the cross product between $\hat{B}_\perp$ and $\hat{R}$, as shown in Figure 5.6. Once the frame is created, we rotate the full uncertainty vector from the Earth RTN frame to the baseline frame, project it onto $\hat{B}_\perp$, and convert it in seconds, to finally obtain σ_{Rel_B}. The injected noise and corresponding weight assigned to the i-th simulated ΔDOR observable will then be given by:

$$\sigma_i = \sqrt{\sigma^2_{RSS,i} + \sigma^2_{Rel_B}} \tag{5.20}$$

Figure 5.7 shows a comparison between the instrumental and mutual orbit uncertainty contributions, both expressed in km, as function of the epoch. Contrary to pseudo-range measurements, the largest contribution is given by the instrumental noise which ranges between 300 and 700 m, while the mutual orbit reaches meter and sub-meter levels of uncertainty.

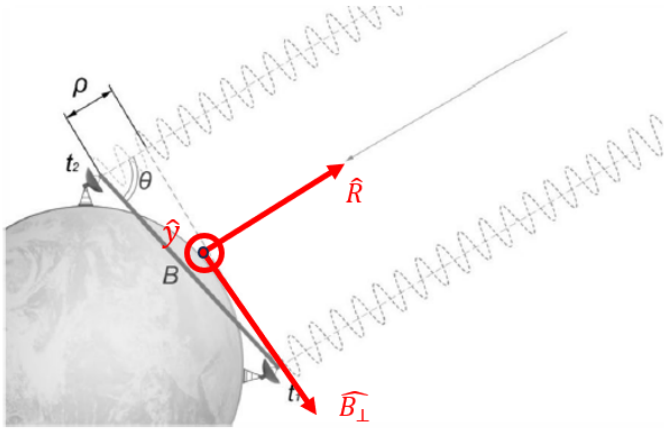

Figure 5.6. Visualization of the Baseline frame.

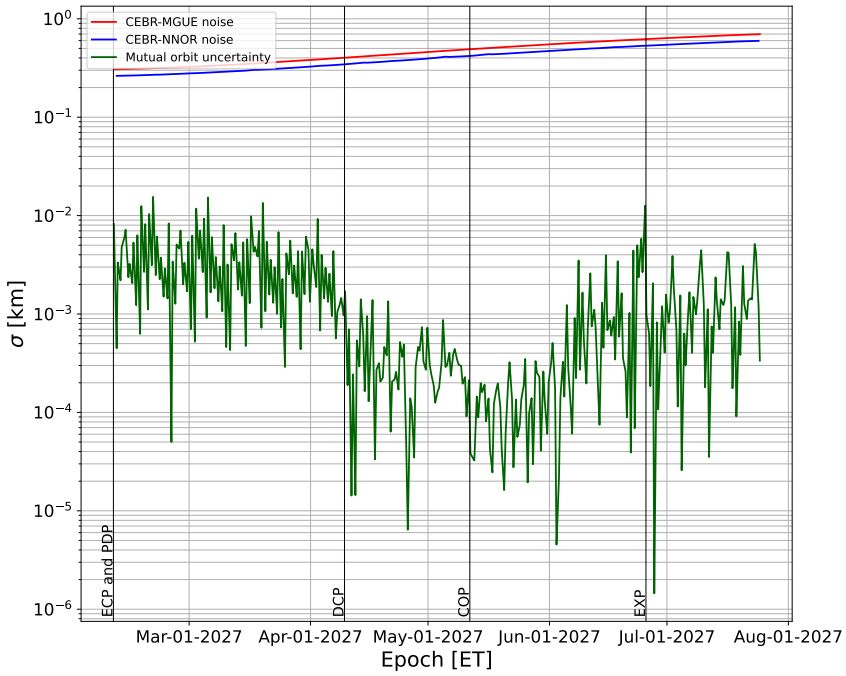

Figure 5.7. Comparison between the instrumental and mutual orbit uncertainties as function of the epoch.

Chapter 6

Covariance analysis

In this chapter, we present a covariance analysis to address how the solution uncertainty is affected by the type of processed measurements. We therefore define a set of future observation scenarios ad we conduct the OD process using the set-up outlined in Chapter 4.3. We emphasize again that we are not interested in the actual values derived for the set of solve-parameters, but we are rather interested in evaluating the variation in the parameters' uncertainties and signal-to-noise-ratios between the cases, with particular attention given to A_2 and $\beta_\odot$.

6.1 Global measurements data set

As we stated earlier, daily ΔDOR observations from both baselines are not a realistic scenario. For this reason in the covariance analysis that we present in this chapter, we reduced the number of ΔDOR measurements to 6, 3 for each baseline. This consideration, together with the simulation procedure that we discussed in the previous chapter, yields a global set of 5892 measurements that includes converted and simulated astrometric observables, synthetic two-way range, and ΔDOR

measurements. Table 6.1 summarizes the final data set specifying the number of measurements for each type. From the whole set we define three cases, each one characterized by a different sub-set of observables.

- Case 1: Only astrometric and radar measurements.
- Case 2: Astrometric, radar, and pseudo-range measurements.
- Case 3: Astrometric, radar, pseudo-range, and ΔDOR measurements.

Figure 6.1 shows the measurement residuals for the considered simulation scenario. The higher uncertainty for the most recent radar delay observations is attributed to the absence of correction using the shape model published by Naidu et al. [18]. Moreover, we point out that during the initial phases of the Hera mission, pseudo-range measurement uncertainties are greater, coherently with the computed mutual orbit uncertainties, which are also higher during that period (Figure 5.3).

Msr No.	**Type**	**First point (TAI)**	**Last point (TAI)**
9	Radar Delay	14-NOV-2003 09:00:32	08-OCT-2022 12:50:37
3891	Pre-Impact Angle Ra-Dec	11-APR-1996 06:42:33	26-SEP-2022 23:15:00
1951	Post-Impact Angle Ra-Dec	26-SEP-2022 23:17:30	15-MAY-2027 21:25:09
46	Hera Two-way range	11-FEB-2027 17:27:07	24-JUL-2027 15:30:07
6	Hera ΔDOR	22-MAR-2027 19:42:37	13-JUN-2027 10:24:07
5903		11-APR-1996 06:42:33	24-JUL-2027 15:30:07

Table 6.1. Global data set.

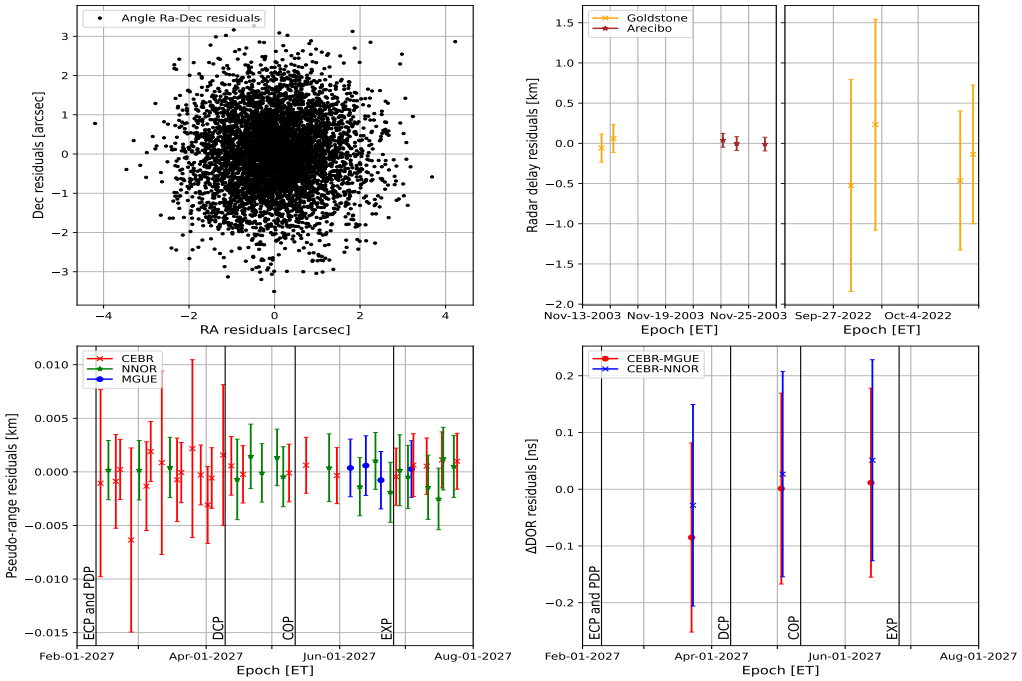

Figure 6.1. Residuals of ground-based optical Right Ascension and Declination (top left panel), radar delay (top right panel), pseudo-range points (bottom left panel), and ΔDOR (bottom right). For the latter three data types, vertical bars corresponding to 3σ uncertainty are also reported.

6.2 Cases comparison

Figure 6.2 shows a comparison of Didymos' position uncertainties for the three cases. We propagate again the solutions' covariance matrix through the whole integration arc, and we express the uncertainties in the Sun RTN frame. From Figure 6.2 we can observe that the introduction of radiometric measurements reduces the position uncertainties by several orders of magnitude, with the best performances shown, as expected, in case 3. This behavior is particularly evident in the radial and transverse direction, where the uncertainty drops to meter and sub-

meter levels during the Hera mission, due to the much higher accuracy of radiometric observables with respect to astrometric measurements. Moreover, we find that this effect is not restricted only to the period of the Hera mission, but it also reflects on the whole duration of the integration arc, with the uncertainties that are reduced by one order of magnitude in cases 2 and 3.

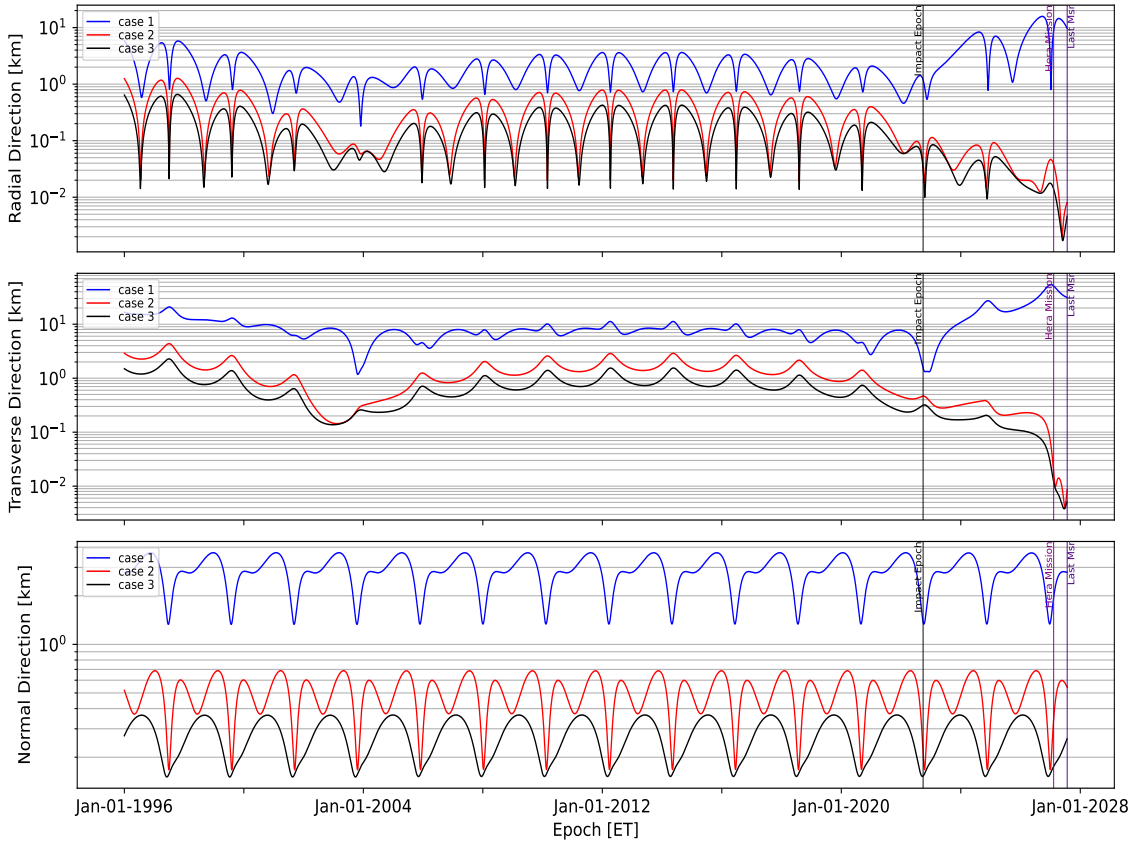

Figure 6.2. Position uncertainty as function of the epoch for the three cases, expressed in the Sun RTN frame in the radial (top), transverse (center) and normal (bottom) directions. The vertical lines drawn in the plots represent the impact epoch, the beginning of the Hera mission, and the last measurement used.

Table 6.2 reports the 1σ uncertainty, and SNR for the parameters A_2 and $\beta_\odot$, which are derived from the 2x2 sub-matrix of the solutions' covariance. We specify that the signal-to-noise ratios presented here and in the next chapter are computed with respect to the value of the parameters associated to the reference solution, which was used for simulating the data.
Although Case 1 shows an improvement in the estimation of $\beta_\odot$ with respect to the results shown in Section 4.3, $\sigma_{\beta_\odot}$ is still too large to obtain a good estimate for the parameter. Case 2 shows a large improvement in the uncertainties of both parameters, with $\text{SNR}_{\beta_\odot}$ that jumps from 0.279 to 5.773, and SNR_{A_2} going from 2.672 to 11.516. Pseudo-range measurements already allow us to obtain a statistically acceptable estimate for $\beta_\odot$ and an accurate estimate for A_2. By comparing Case 2 and 3, we notice that the addition of 6 ΔDOR measurements, spread across the nominal mission phases, nearly doubles both signal-to-noise ratios. Finally, we also reported the A_2 and $\beta_\odot$ correlation coefficient μ for the three cases. The introduction of radiometric measurements increases μ from 0.132 to nearly 1, meaning that the two parameters are highly positively correlated. This highlights the need of accurate estimations to effectively separate the two effects.
The results presented in this section lead us to the conclusion that the parameters estimation, and therefore Didymos' post-impact heliocentric trajectory reconstruction, will largely benefit from the inclusion of ΔDOR measurements in the mission operations. In this scenario, post-Hera OD analyses are expected to determine accurately both parameters and assess very confidently the effects on the heliocentric orbit of DART's impact.

Case	$\sigma_{\beta_\odot}$	$\text{SNR}_{\beta_\odot}$	σ_{A_2} [au/day^2]	SNR_{A_2}	μ
Case 1	10.742	0.279	6.509×10^{-15}	2.672	0.132
Case 2	0.519	5.773	1.510×10^{-15}	11.516	0.993
Case 3	0.317	9.457	8.450×10^{-16}	20.460	0.982

Table 6.2. A_2 and $\beta_\odot$ uncertainty, SNR, and correlation coefficient for the three cases.

Chapter 7

Sensitivity analysis

In the previous chapter, we presented the resulting solution covariance under the assumption that the CEBR-NNOR and CEBR-MGUE baselines will perform 3 ΔDOR measurements across Hera's nominal mission phases. In this section, we explore different ΔDOR operation scenarios and determine how they affect the OD performances. We considered three sub-cases determined by the baseline performing the measurements. In two sub-cases, measurements are provided by either one of the two baselines, while in the final sub-case, both baselines perform the measurements. For each sub-case, we vary the number of observations (N) from 0 to 10 and run the estimation process to derive the solutions' covariance.
Figure 7.1 shows the A_2 and $\beta_\odot$ uncertainty variation as a function of the number of ΔDOR measurements per baseline for the three sub-cases. As expected, $\sigma_{\beta_\odot}$ and σ_{A_2} both decrease as the number of measurements increases. Moreover, the CEBR-NNOR baseline shows better performances with respect to CEBR-MGUE, which is probably due to the lower noise computed for the CEBR-NNOR baseline (Section 5.3.3). We also point out that, for the same total number of measurements, in terms of estimation performances it is more convenient to

employ just the CEBR-NNOR baseline. 6 measurements from CEBR-NNOR provide slightly improved estimation results if compared to the case of 3 measurements from both baselines, showing a 5.70% and 5.36% reduction for σ_{A_2} and $\sigma_{\beta_\odot}$ respectively.
Similar considerations can be made for the SNRs values, which coherently exhibit an increasing trend with the number of observations. Moreover, A_2 proves to be more sensible to ΔDOR measurements with respect to $\beta_\odot$, as it demonstrates larger variations for both uncertainty and SNR. The signal-to-noise ratio of $\beta_\odot$ shows a slow increase with N, seemingly reaching a plateau at N = 9. Although $\text{SNR}_{\beta_\odot}$ may continue to increase with a higher number of measurements, such scenarios are less likely during the mission operations, hence our decision to limit the analysis at N = 10.
In conclusion, while a larger number of observations generally leads to better estimation performance, it's noteworthy that even a small number of ΔDOR measurements, when processed alongside pseudo-range and astrometric observables, can yield good estimates for both parameters. For $\beta_\odot$, just three ΔDOR observations suffice, whereas for A_2, the uncertainty continues to decrease almost linearly as the number of observations increases. From an operational point of view, in the least-effort scenario (N = 1 and single baseline), we already observe a distinct reduction in uncertainty compared to the case with no ΔDOR, with the signal-to-noise ratios of A_2 and $\beta_\odot$ increasing by 24.4% and 21.3%, respectively.

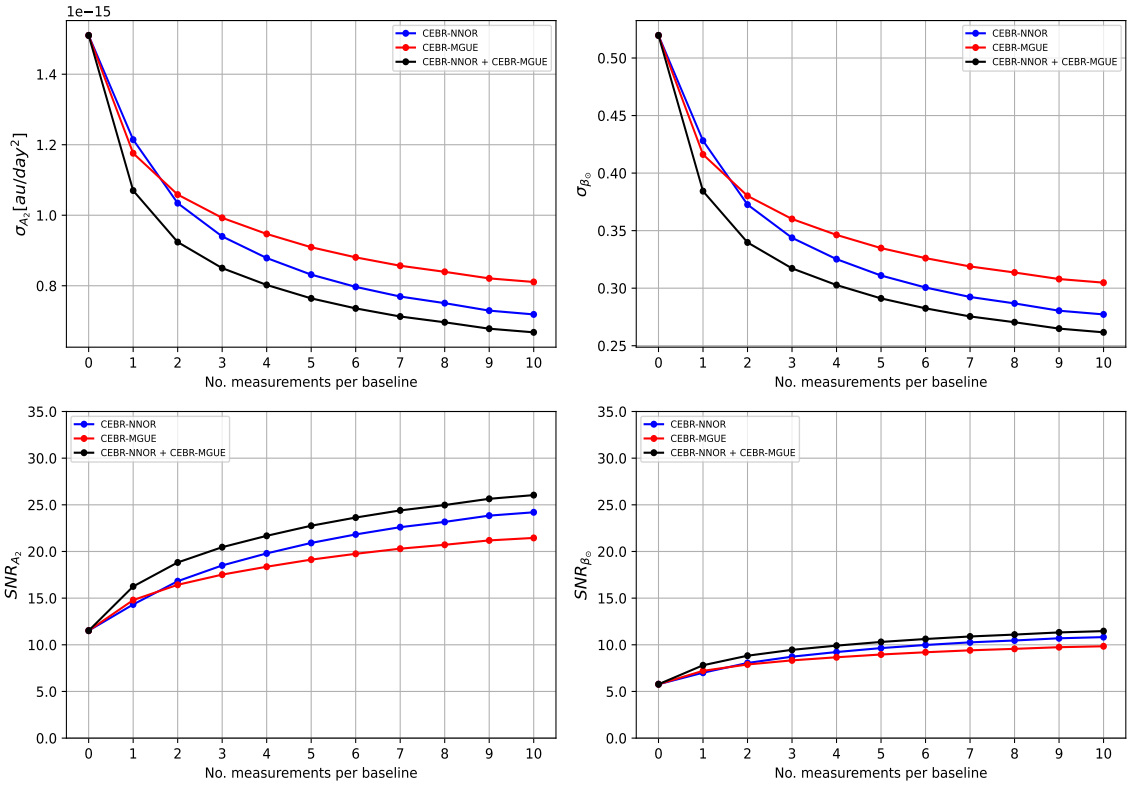

Figure 7.1. A_2 and $\beta_\odot$ uncertainty (top) and SNR (bottom) variation as a function of the number of ΔDOR measurements per baseline performing the observations. Note that the sub-case with 0 measurements is equivalent to Case 2 (using astrometric and pseudo-range measurements only).

Conclusions

This work presented the reconstruction of the heliocentric trajectory of Didymos. Initially, we validated the model by fitting the currently available observations of the asteroid and comparing the solution to previous results from the literature. We found that current information is insufficient to obtain an acceptable estimate for the $\beta_\odot$ parameter. This is likely due to the low number of observations collected after DART's impact, and the poor information content given by astrometric measurements, which are not accurate enough to detect small effects like the impact-induced ΔV.
We therefore explored the observability of the parameters under different observation scenarios, which included future ground-based astrometric observations and measurements collected by the upcoming Hera mission, namely pseudo-range and ΔDOR observables. Under the nominal scenario, which considers one pseudo-range measurement per Hera orbit determination arc and 3 ΔDOR measurements for each baseline during the course of the mission, we found that the introduction of radiometric measurements reduces by two orders of magnitudes the asteroid position uncertainties and largely improves the parameters estimation, with SNRs reaching values of 9.5 and 20.5 for $\beta_\odot$ and A_2 respectively. Furthermore, we explored the sensitivity of the estimated parameters to different ΔDOR operation scenarios. We found that the CEBR-NNOR baseline demonstrates overall better performance, while

incorporating the CEBR-MGUE baseline, alongside the other, provides only a negligible difference. The improvement in the uncertainty levels tends to reduce after a limited number of measurements. For $\beta_{\odot}$, three ΔDOR observations are already enough, while for A_2 the uncertainty continues to drop almost linearly as the number of measurements increases. In particular, we found that one observation from a single baseline is already enough to increase considerably A_2 and $\beta_{\odot}$ signal-to-noise ratios respectively by 24.4% and 21.3%, if compared to the case with no ΔDOR.
Given the high correlation between the two non-gravitational effects, we therefore conclude that the addition of ΔDOR observations to the mission operations would enhance the post-Hera orbit determination. This would allow us to accurately reconstruct the heliocentric trajectory of the Didymos system, and evaluate the momentum transferred during a kinetic impact. Consequently, we would be able to effectively model and predict the efficacy of potential future planetary defense missions utilizing kinetic-impactor techniques.

Bibliography

[1] Nikola Schmidt. *Planetary Defense. Global Collaboration for Defending Earth from Asteroids and Comets*. Gewerbestrasse 11, 6330 Cham, Switzerland: Springer Nature Switzerland, 2019.

[2] Minor Planet Center. *Didymos (65803) data*. `https://cgi.minorplanetcenter.net/db_search/show_object?object_id=65803`. Accessed: 2023-04-14.

[3] Andrew F Cheng et al. "AIDA DART asteroid deflection test: Planetary defense and science objectives". In: *Planetary and Space Science* 157 (2018), pp. 104–115.

[4] Andrew S Rivkin et al. "The double asteroid redirection test (DART): Planetary defense investigations and requirements". In: *The Planetary Science Journal* 2.5 (2021), p. 173.

[5] Cristina A Thomas et al. "Orbital period change of Dimorphos due to the DART kinetic impact". In: *Nature* (2023), pp. 1–3.

[6] Andrew F Cheng et al. "Momentum transfer from the DART mission kinetic impact on asteroid Dimorphos". In: *Nature* 616.7957 (2023), pp. 457–460.

[7] Rahil Makadia et al. "Heliocentric effects of the DART mission on the (65803) Didymos binary asteroid system". In: *The planetary science journal* 3.8 (2022), p. 184.

[8] Patrick Michel et al. “The ESA Hera mission: detailed characterization of the DART impact outcome and of the binary asteroid (65803) Didymos”. In: *The Planetary Science Journal* 3.7 (2022), p. 160.

[9] “Astrometry of asteroids”. In: *Deparment of physics, Gettysburg College. Gettysburg, PA 17325* ().

[10] Peter Vereš et al. “Statistical analysis of astrometric errors for the most productive asteroid surveys”. In: *Icarus* 296 (2017), pp. 139–149.

[11] SJ Ostro et al. “Asteroid radar astrometry”. In: *Astronomical Journal (ISSN 0004-6256), vol. 102, Oct. 1991, p. 1490-1502. Research supported by NASA.* 102 (1991), pp. 1490–1502.

[12] Radiometric Tracking Techniques For Deep Space Navigation. *Catherine L. Thornton, James S. Border.* John Wiley Sons. Inc, 2003.

[13] P.W. Kinman. *DSN Telecommunications Link, Design Handbook. Sequential Ranging.* California Institute of Technology, 2009.

[14] Francesco Fiori et al. “Deep space orbit determination via Delta-DOR using VLBI antennas”. In: *CEAS Space Journal* 14.2 (2022), pp. 421–430.

[15] Harald Schuh and Dirk Behrend. “VLBI: A fascinating technique for geodesy and astrometry”. In: *Journal of geodynamics* 61 (2012), pp. 68–80.

[16] CCSDS 500.1-G-2. *DELTA-DOR TECHNICAL CHARACTERISTICS AND PERFORMANCE.* Tech. rep. CCSDS; The consultive Commitee for Space Data Systems, November 2019.

[17] Steven R Chesley, James Baer, and David G Monet. “Treatment of star catalog biases in asteroid astrometric observations”. In: *Icarus* 210.1 (2010), pp. 158–181.

[18] SP Naidu et al. "Radar observations and a physical model of binary near-Earth asteroid 65803 Didymos, target of the DART mission". In: *Icarus* 348 (2020), p. 113777.

[19] Andrea Milani and Giovanni Gronchi. *Theory of orbit determination*. Cambridge University Press, 2010.

[20] William F Bottke Jr et al. "The Yarkovsky and YORP effects: Implications for asteroid dynamics". In: *Annu. Rev. Earth Planet. Sci.* 34 (2006), pp. 157–191.

[21] Shantanu Naidu Steven R. Chesley Davide Farnocchia. "Asteroid (65803) Didymos Ephemeris Delivery, JPL Solution 181". In: (February 17, 2021).

[22] D. Farnocchia. "Small-Body Perturber Files SB441-N16 and SB441-N343". In: (March 30, 2021).

[23] Brian G Marsden, Z Sekanina, and DK Yeomans. "Comets and nongravitational forces. V". In: *The Astronomical Journal* 78 (1973), p. 211.

[24] Davide Farnocchia et al. "Near Earth asteroids with measurable Yarkovsky effect". In: *Icarus* 224.1 (2013), pp. 1–13.

[25] Siegfried Eggl et al. "Star catalog position and proper motion corrections in asteroid astrometry II: The Gaia era". In: *Icarus* 339 (2020), p. 113596.

[26] Mario Carpino, Andrea Milani, and Steven R Chesley. "Error statistics of asteroid optical astrometric observations". In: *Icarus* 166.2 (2003), pp. 248–270.

[27] R Terik Daly et al. "Successful kinetic impact into an asteroid for planetary defence". In: *Nature* 616.7957 (2023), pp. 443–447.

[28] Davide Farnocchia et al. "High-fidelity comet 67P ephemeris and predictions based on Rosetta data". In: *Icarus* 358 (2021), p. 114276.

[29] AS Konopliv et al. “The Vesta gravity field, spin pole and rotation period, landmark positions, and ephemeris from the Dawn tracking and optical data”. In: *Icarus* 240 (2014), pp. 103–117.

[30] “The H and G magnitude system for asteroids”. In: 2007.

[31] Edoardo Gramigna et al. “The hera radio science experiment at didymos”. In: *arXiv preprint arXiv:2310.11883* (2023).

[32] David W Curkendall and James S Border. “Delta-DOR: The one-nanoradian navigation measurement system of the deep space network—History, architecture, and componentry”. In: *The Interplanetary Network Progress Report* 42 (2013), p. 193.

[33] Christopher S Jacobs, Task Lead, and Peter Kroger. “X-Band Radio Source Catalog”. In: *DSN Telecommunications Link Design Handbook* (2015), pp. 810–005.